

PAPER

[View Article Online](#)
[View Journal](#) | [View Issue](#)Cite this: *Nanoscale Adv.*, 2025, 7, 5760

Synthesis, molecular docking, pharmacological evaluation, MD simulation, and DFT calculations of quinazolin-12-one derivatives as PDK1 inhibitors†

Zahra Sadeghian,^a Mohammad Bayat ^{*a} and Davood Gheidari ^{*b}

3-Phosphoinositide-dependent protein kinase-1(PDK1) is a vital kinase in cellular signaling that regulates growth and survival, playing a crucial role in cancer by activating Akt within the PI3K/Akt pathway. Elevated PDK1 levels correlate with tumor progression and chemotherapy resistance, highlighting its potential as a therapeutic target and biomarker. Schiff bases (SBs) are widely utilized as anticancer agents, as well as for antiviral, antipyretic, antimicrobial, antifungal, antiproliferative, and anti-inflammatory purposes. In this study, we synthesized a series of new quinazolin-12-one derivatives with moderate to good yields (72–92%) and evaluated their efficacy against PDK1 using *in silico* methods. Comprehensive computational studies, including quantum chemical calculations, molecular docking, molecular dynamics (MD), and absorption, distribution, metabolism, excretion, and toxicity (ADMET) profiling, were performed. Density functional theory (DFT) analysis with the B3LYP/6-31++G (d, p) basis set indicated a promising reactivity profile for the synthesized compounds. The oxygen atoms and π -system of the title compound exhibit high chemical reactivity, serving as electron donor sites and targets for electrophilic attack. Docking analysis with PDK1 enzymes revealed that all compounds, with docking scores between -9.99 and -10.44 , demonstrated greater binding affinity than the native ligand, which had a score of -9.49 . Among these, compound **3f**, with an energy of -10.44 kcal mol⁻¹, displayed the strongest binding affinity. The MD simulation showed that Ala162 stands out with a notably high interaction fraction, suggesting that it may be a critical residue for the binding affinity of compound **3f**. The analysis of ADMET properties indicated that all inhibitor compounds exhibit favorable pharmacological characteristics, including adherence to Lipinski's Rule of Five (Ro5) as well as the Ghose, Veber, and Egan rules. Additionally, the physicochemical properties demonstrate that all synthesized compounds are capable of human intestinal absorption and have the ability to penetrate the blood–brain barrier (BBB).

Received 24th February 2025
Accepted 21st July 2025

DOI: 10.1039/d5na00182j

rsc.li/nanoscale-advances

Introduction

The global burden of cancer continues to rise at an alarming rate, with the International Agency for Research on Cancer (IARC) projecting that the number of new cancer cases will reach approximately 29.5 million by 2040, representing a staggering 47% increase from the estimated 19.3 million cases in 2020.¹ Factors such as population growth, aging, and lifestyle changes contribute to this increase, emphasizing the urgent need for innovative therapeutic strategies to combat this escalating health crisis. PDK1 is a key member of the AGC kinase family, which comprises serine and threonine kinases that

demonstrate sequence homology in their catalytic domains with cAMP-dependent protein kinase A (PKA), cGMP-dependent protein kinase (PKG), and protein kinase C (PKC).² The structure of the catalytic domain includes an amino-terminal small lobe and a carboxy-terminal large lobe, which together bind a single ATP molecule essential for subsequent substrate phosphorylation.² Most AGC kinases possess two phosphorylation sites that regulate their activation: the activation loop within the kinase domain and the hydrophobic motif located adjacent to the catalytic domain. Phosphorylation at these sites enhances kinase activity, leading to full enzymatic activation. However, PDK1 is inherently active, with its regulation occurring through alternative mechanisms. One critical mechanism involves the localization of PDK1 at the plasma membrane, which was identified during studies analyzing Akt T-loop phosphorylation in living cells. The interaction of PDK1's pleckstrin homology (PH) domain with phosphoinositides, such as PtdIns(3,4,5)P₃, phosphatidylinositol 3,4-bisphosphate (PtdIns(3,4)P₂), and PtdIns(4,5)P₂ enhances this localization,

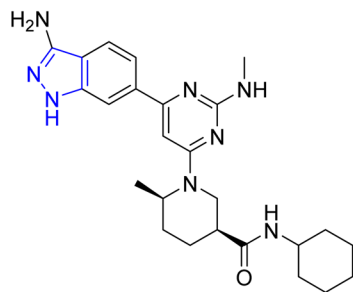
^aDepartment of Chemistry, Faculty of Science, Imam Khomeini International University, Qazvin, Iran. E-mail: m.bayat@sci.ikiu.ac.ir^bDepartment of Chemistry, Faculty of Science, University of Guilan, Rasht, Iran. E-mail: davoodgheidari@gmail.com† Electronic supplementary information (ESI) available. See DOI: <https://doi.org/10.1039/d5na00182j>

exhibiting the highest affinity for lipid products of PI3K.³ While PDK1 was initially recognized for its role in phosphorylating Akt, it is now established that numerous other kinases are also downstream targets of PDK1. AGC kinases, including serum glucocorticoid-dependent kinase (SGK), p70 ribosomal protein S6 kinases (S6K), p90 ribosomal protein S6 kinase (RSK), and atypical PKC isoforms, are directly phosphorylated by PDK1 at specific serine/threonine residues in their activation loops.⁴ As a result, PDK1 is often termed the “master regulator” of AGC kinase signaling, playing a central role in controlling cell proliferation, survival, and motility.⁴ Additionally, hyperactivation of the PI3K/PDK1/Akt pathway is linked to various human cancers. The significance of PDK1 extends beyond its basic cellular signaling functions; it also plays a pivotal role in chemoresistance and survival pathways across multiple cancer types. PDK1 is instrumental in activating key signaling pathways that bolster cancer cell survival during chemotherapy. Specifically, PDK1 promotes the phosphorylation and activation of Akt, a downstream effector crucial for mediating anti-apoptotic signals. Increased Akt activity can render chemotherapeutic agents less effective by inhibiting pro-apoptotic factors and activating anti-apoptotic proteins, ultimately increasing cancer cell survival rates. For example, studies have shown that cancer cells with elevated PDK1 levels exhibit significant resistance to chemotherapeutics such as doxorubicin and paclitaxel, leading to treatment failures in patients.⁵ Targeting PDK1 has emerged as a promising approach to enhance drug sensitivity in cancer therapy. Recent research indicates that the inhibition of PDK1 can significantly increase the efficacy of chemotherapeutic agents, particularly gemcitabine in pancreatic cancer models, where PDK1 inhibition sensitizes cancer cells to drug-induced apoptosis.⁶ This finding underscores the potential of downgrading the PI3K/PDK1/Akt pathway to improve therapeutic outcomes by countering resistance mechanisms. Additionally, PDK1 is critical in the epithelial-mesenchymal transition (EMT), which is significantly associated with increased chemoresistance. By facilitating enhanced migratory capacity and invasive properties of cancer cells, EMT contributes to their resistance against apoptosis. Modulation of PDK1 during EMT promotes the metastatic dissemination of cancer and the development of therapy resistance.⁷ For instance, high PDK1 levels in breast cancer correlate with poor prognosis and resistance to trastuzumab.⁸ In ovarian cancer, PDK1 has been implicated in the development of carboplatin resistance through alterations in critical survival pathways.⁹ Given its substantial involvement in promoting chemoresistance, targeting PDK1 is being actively investigated as a potential strategy to overcome drug resistance and enhance chemotherapy effectiveness. Recent studies have increasingly focused on developing pharmacological inhibitors of PDK1, which are currently being evaluated in preclinical models to enhance existing cancer therapies.¹⁰ This trend in drug design aims to achieve more precise mechanisms of cancer cell destruction, thereby minimizing the adverse effects associated with cancer treatment. In the pursuit of investigating chemical substances with properties suitable for designing novel anticancer agents, special attention has been directed

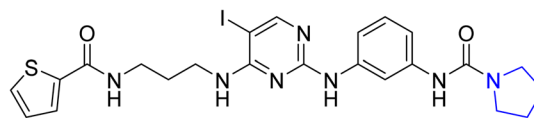
toward heterocyclic aromatic compounds containing nitrogen, which are well recognized for their therapeutic potential. Fig. 1 illustrates several PDK1 inhibitors, including nitrogen-containing heterocycles such as GSK2334470, BX-795, OSU-03012, BX-912, and (3Z)-3-(1H-pyrrol-2-ylmethylene)-1,3-dihydro-2H-indol-2-one. All of these compounds feature a five-membered nitrogen-containing ring, suggesting their efficacy and therapeutic properties that enhance interactions with biological targets. This characteristic positions them as promising candidates for research in cancer treatment. Among these compounds, indole dione derivatives are particularly noteworthy; one of their dione groups undergoes a condensation reaction, leading to the synthesis of various biologically active compounds.¹¹

These compounds represent the core structure of sunitinib, a well-known multi-kinase inhibitor.¹² The compound (Z)-3-((1H-pyrrol-2-yl)methylene)indolin-2-one was identified as a promising lead through high-throughput screening with a PDK1-mediated Akt2 activation assay (cAKT2), demonstrating the ability to inhibit Akt2 activation in the low micromolar range.¹³ Additionally, it effectively prevented Akt activation in tumor cells. Despite these promising results, it exhibited reduced potency against PKA, which is structurally similar. This limitation prompted the optimization process that yielded the compound BX-517. Detailed X-ray crystallographic analysis of BX-517 within the ATP binding pocket of PDK1 revealed its precise binding interactions. The pyrrole-indolinone core forms three significant hydrogen bonds with the hinge region of PDK1. Specifically, the nitrogen of the indolinone interacts with the carbonyl group of Ser160, while the indolinone's oxygen accepts a hydrogen bond from the amide of Ala162. Additionally, the nitrogen in the pyrrole ring interacts with the carbonyl of Ala162, albeit in a geometrically unfavorable manner. The 5-position urea group engages in hydrogen bonding with both the side chain of Lys111 and the hydroxyl group of Thr222. Notably, the interaction with Thr222 may contribute to the selectivity of BX-517 for PDK1. However, BX-517 presents significant challenges in its ADME profile, characterized by a short half-life, low metabolic stability, and poor solubility in aqueous environments, which hampered its further development.¹⁴ As a result, subsequent efforts in medicinal chemistry led to the discovery of more potent compounds, such as (Z)-1-(2-oxo-3-(pyridin-3-yl(1H-pyrrol-2-yl)methylene)indolin-5-yl)urea. This compound demonstrated enhanced overall performance in enzyme and cellular assays, along with improved pharmacokinetic properties. Nevertheless, it only exhibited twofold selectivity for PDK1 over PKA, significantly lower than the initial lead compound's impressive 320-fold selectivity for (Z)-3-((1H-pyrrol-2-yl)methylene)indolin-2-one. In parallel, another significant class of compounds known as SBs has garnered considerable attention in recent years. These versatile organic compounds are synthesized through the condensation of primary amines with carbonyl compounds, resulting in the formation of imines. SBs are particularly noteworthy for their diverse biological activities, which include anticancer, antiviral, antimicrobial, and anti-inflammatory properties, making them valuable in medicinal chemistry. Additionally, their stability and ability to form strong

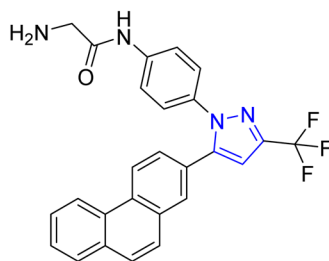




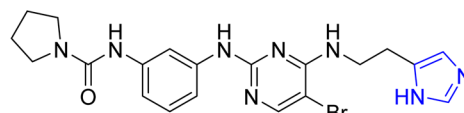
GSK2334470



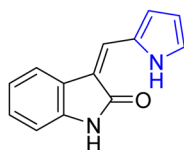
BX-795



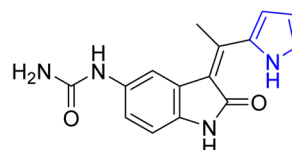
OSU-03012



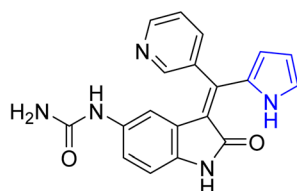
BX-912



(Z)-3-((1H-pyrrol-2-yl)methylene)indolin-2-one



BX-517



(Z)-1-(2-oxo-3-(pyridin-3-yl)methylene)indolin-5-yl)urea

Fig. 1 Some PDK1 inhibitors contain a five-membered N-containing ring.

complexes with metal ions enhance their therapeutic potential and broaden their industrial applications.¹⁵ Synthesized through the condensation of a primary amine with a carbonyl group, SBs form an imine functional group that plays a crucial role in various biological processes. Their ability to form stable complexes with metal ions enhances their therapeutic potential.¹⁶ SBs are widely utilized as anticancer agents, as well as for antiviral, antipyretic, antimicrobial, antifungal, anti-proliferative, and anti-inflammatory purposes.^{17–21} The unique functionality of the azomethine group, characterized by a lone pair of electrons in a sp^2 hybridized orbital of the nitrogen atom

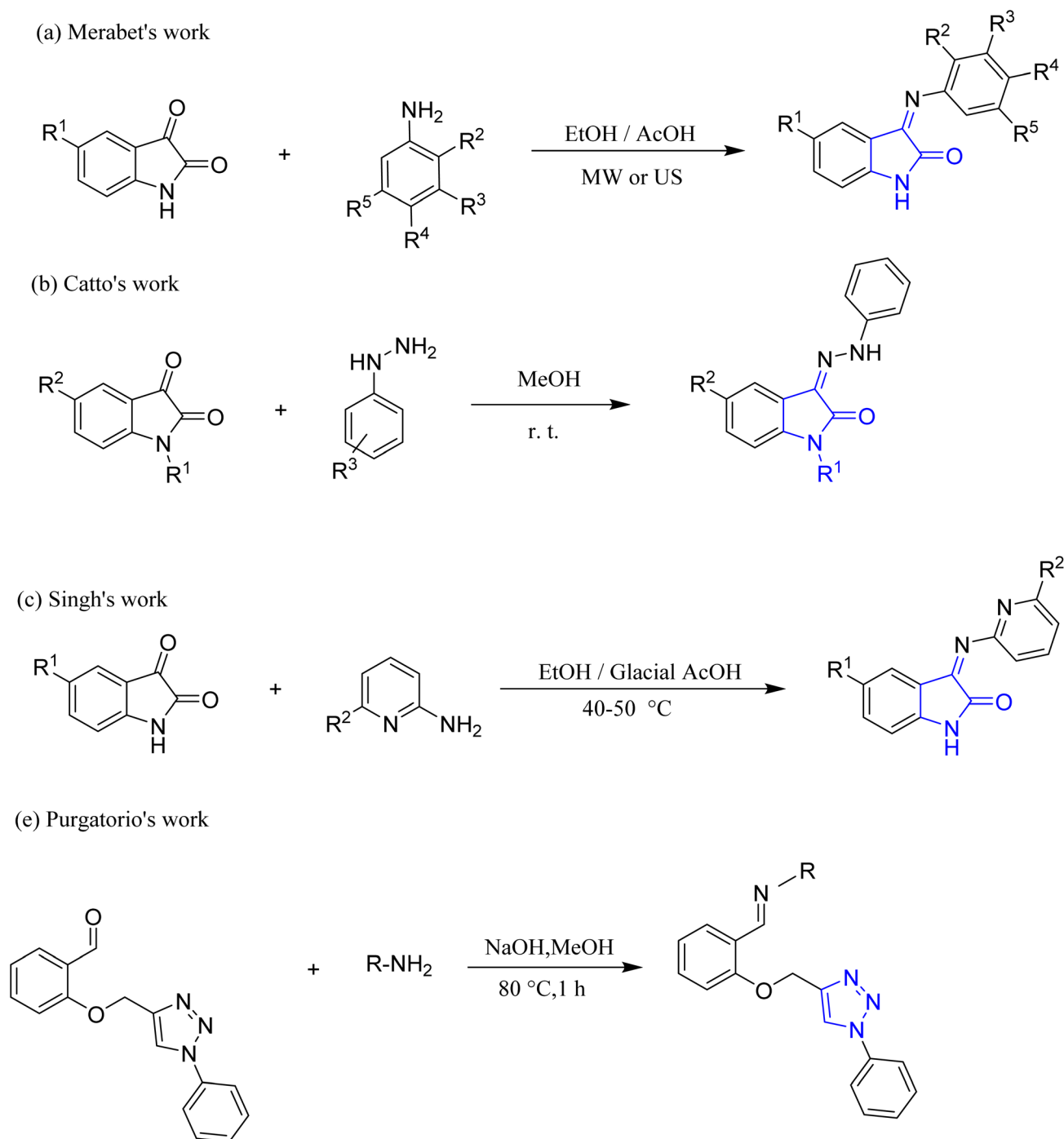
and fused to a five-membered nitrogen-containing ring, significantly contributes to the diverse biological activities of Schiff base molecules. This combination not only enhances the electronic properties of the molecules but also facilitates stronger interactions with biological targets, ultimately improving their therapeutic effectiveness. The strong binding interactions between the electrophilic carbon and nucleophilic nitrogen in the imine ($-C=N-$) bond facilitate effective interactions with various nucleophiles and electrophiles, thereby inhibiting specific diseases, enzymes, or DNA replication.²² Due to their straightforward synthesis, flexibility, and wide range of



applications, SBs have attracted significant interest from chemical researchers. For example, Merabet *et al.* synthesized antimicrobial compounds using SBs formed between isatins and various anilines *via* a green procedure (Scheme 1a).²³ Meanwhile, Catto *et al.* developed arylhydrazones from isatins or *N*-methylisatins with corresponding arylhydrazines in methanol at room temperature as anti-amyloidogenic agents (Scheme 1b).²⁴ In 2021, Singh *et al.*²⁵ demonstrated the antibacterial potential of pyridin-2-amine through SBs derived from isatins (Scheme 1c). More recently, in 2024, Belay *et al.*²⁶

reported the synthesis of chiral SBs from benzaldehyde as anticancer agents (Scheme 1d).

Consequently, scientists are increasingly interested in the creation and synthesis of SBs through condensation techniques involving suitable carbonyl groups. Based on previous research on bioactive heterocyclic compounds,²⁷ we conducted a study on the synthesis of SBs *via* tryptanthrin. Considering the importance of bioinformatics methods such as molecular docking and MD simulation, we simulated these compounds in relation to target receptors, providing insights into their



Scheme 1 Various methods for the synthesis of SBs.

similarities and binding characteristics. This approach is highly valuable for screening compounds and identifying those with promising biological activity, serving as a powerful tool for analyzing biological data and predicting molecular interactions. Its ability to model interactions at the atomic level accelerates the drug discovery process while reducing reliance on time-consuming experimental methods. Also, we utilized DFT analyses, which are fundamental aspects of computational chemistry. DFT provides a quantum mechanical description of electronic structures and enables the prediction of molecular geometries, electronic properties, and reaction mechanisms with high accuracy.²⁸ It is particularly effective in elucidating the energetics of molecular interactions, which is crucial for understanding binding affinities and stability in drug design.

Results and discussion

Chemistry

We have developed a simple and efficient method for producing quinazolin-12-one derivatives (**3a–l**) through a one-step reaction. To optimize the reaction conditions, we explored the reaction of tryptanthrin (**1a–c**), synthesized from isatins and isatoic anhydride, with arylhydrazine hydrochloride (**2a**) under various conditions.²⁹ Initially, water was selected as a green solvent, but the reaction did not proceed in this medium (entry 1, Table 1). Raising the temperature to reflux in water resulted in a poor yield (entry 2, Table 1). The use of methanol or ethanol produced only modest yields (entries 3–6, Table 1). Consequently, we identified CH₃CN as the optimal solvent at reflux temperature (entry 7, Table 1). Under these conditions, we successfully synthesized the desired compounds (**3a–l**) by reacting tryptanthrin (**1a–c**) with arylhydrazine hydrochloride (**2a**). The results revealed that tryptanthrin featuring a chloro

substituent produced the greatest amount of product when reacted with all arylhydrazine hydrochloride derivatives, specifically compounds (**3b**), (**3e**), (**3h**), and (**3j**). Additionally, the use of unsubstituted phenylhydrazine hydrochloride in reactions with various tryptanthrins resulted in the formation of compound (**3b**) with higher yields.

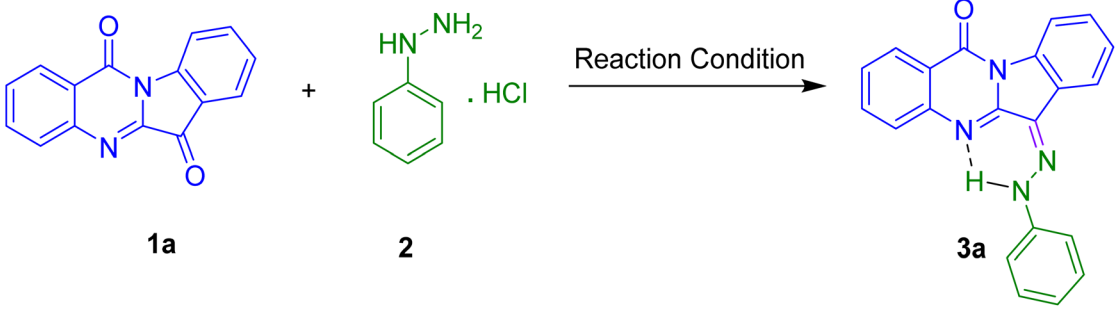
The detailed structures of the synthesized derivatives are provided in Fig. 2. The ¹H NMR spectra of compound (**3a**) showed chemical shifts ranging from δ 13.49 to 8.46–7.11 ppm. The singlet at δ 13.49 ppm corresponds to the amino proton, while the range of δ 8.46–7.11 ppm is indicative of aromatic protons. The ¹³C NMR spectra showed signals at 158.5, 146.7, 148.5, 142.6, 142.5, and 136.9 ppm, corresponding to (C=O), (N=C–N), (C=N), (C–NH), and (N–C=) bonds. Additionally, the signals in the range of 114.5 to 134.1 ppm correspond to aromatic C atoms. Furthermore, stretching vibrations corresponding to the (NH), (=CH), and (C=O) groups were observed at 3100, 3035, and 1678 cm^{−1}, respectively. Other prominent bands at wavenumbers of 1599, 1544, 1466, 1315, 1249, 1174, and 755 cm^{−1} are associated with groups comprising (C=C), (C–N), (C–NH), (C–N), and (Ar), respectively. The spectral data provided conclusive evidence of the production of the intended molecule.

The possible mechanism for the generation of compound (**3a**) is presented in Scheme 2. It is believed that hydrogen chloride activates the carbonyl group in tryptanthrin (**1a**) through protonation. Then the nucleophilic addition of phenylhydrazine (**2a**), followed by dehydration, leads to the formation of the final product (**3a**).

Computational studies

DFT calculations. All DFT calculations for the synthesized quinazolin-12-one derivatives (**3a–l**) were performed using Gaussian 09W software at the B3LYP/6-31++G(d,p) level of

Table 1 Optimized reaction conditions for the production of compound (**3a**)

				
Entry	Solvent	Temperature (°C)	Time (h)	Yield (%)
1	H ₂ O	25	24	No reaction
2	H ₂ O	Reflux	24	30
3	EtOH	25	24	50
4	EtOH	Reflux	24	55
5	MeOH	25	24	51
6	MeOH	Reflux	15 min	56
7	CH ₃ CN	Reflux	15 min	74



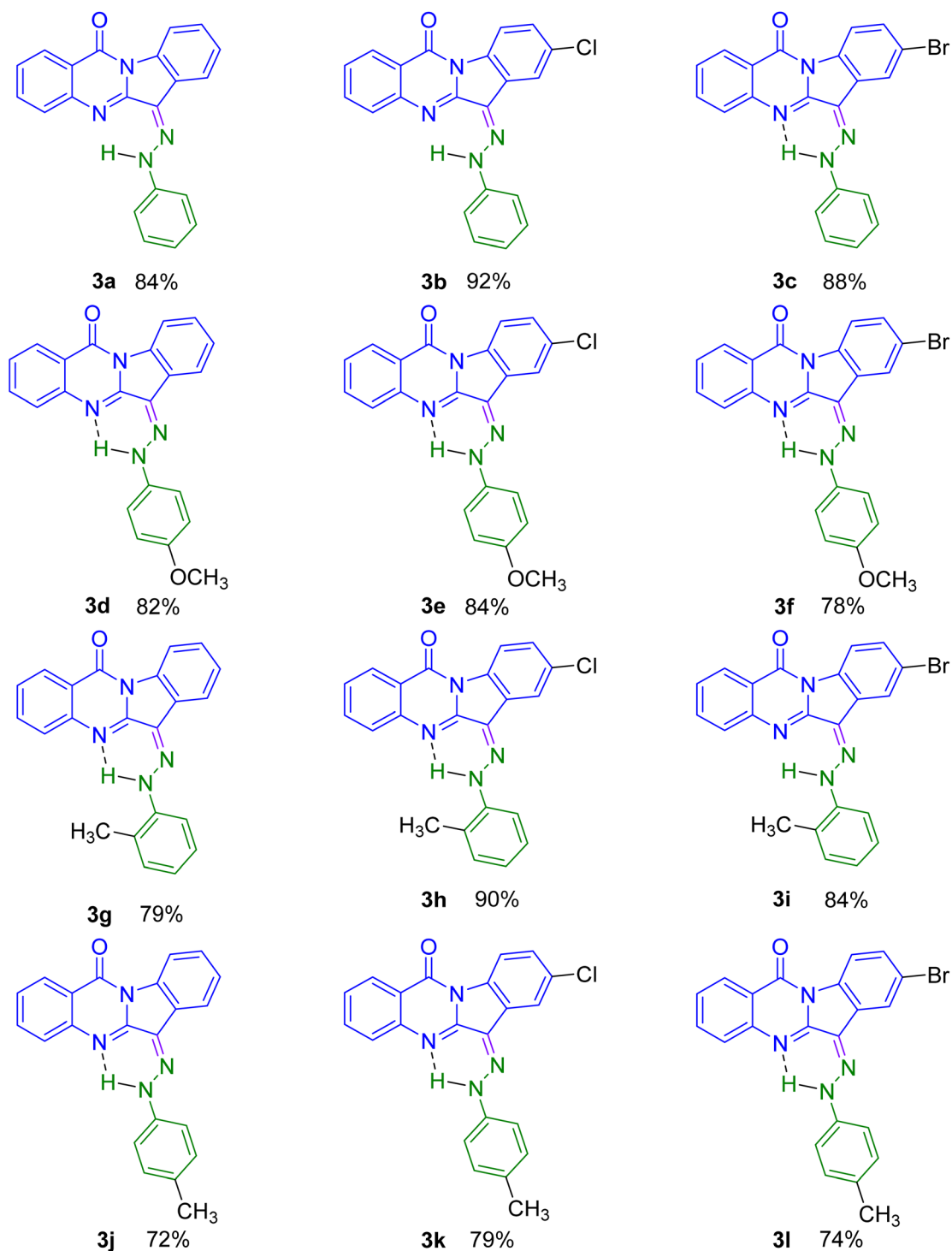
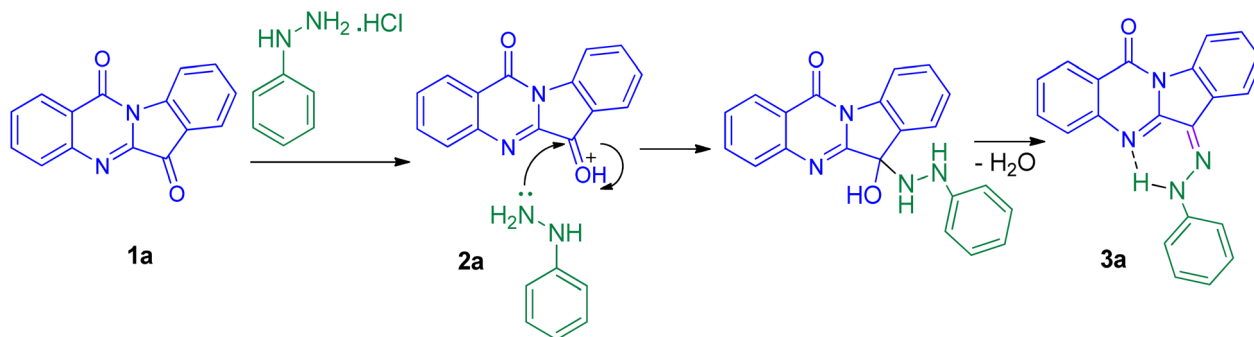


Fig. 2 The molecular structures with yields of the compounds (3a–l).

theory. The parameters for each compound are presented in Table 2.

The present investigation aimed to estimate a range of molecular properties and reactivity descriptors based on the energies of frontier molecular orbitals (FMOs).³⁰ The reactivity of the compounds was assessed by estimating three key parameters: the energy of the highest occupied molecular

orbital (HOMO), the energy of the lowest unoccupied molecular orbital (LUMO), and the energy gap between the HOMO and LUMO. These parameters help establish the reactivity order of the produced compounds (3a–l). The HOMO energy indicates a molecule's ability to donate electrons, while the LUMO energy reflects its ability to accept electrons. The FMOs of the synthesized derivatives are illustrated in Fig. 3.



Scheme 2 Possible mechanism for the generation of indolo[2,1-*b*]quinazolin-12-one (**3a**).

Table 2 Geometric parameters of the compounds (**3a**–**l**)

Compound	Gas phase		
	Optimization energy (hartree)	Polarizability (α) (a.u.)	Dipole moment (Debye)
3a	−1102.9839	340.7526	2.9307
3b	−1562.5772	358.0203	4.5774
3c	−3674.1128	368.4893	4.5731
3d	−1217.5116	372.5910	4.8428
3e	−1677.1050	390.9570	6.5568
3f	−3788.6407	401.4916	6.5657
3g	−1142.3040	352.2846	3.0246
3h	−1601.8973	369.8366	4.8176
3i	−3713.4329	380.1256	4.8159
3j	−1142.3046	361.0400	3.6578
3k	−1601.8980	378.6250	5.1276
3l	−3713.4336	388.9030	5.1401

Table 3 provides a comprehensive overview of other calculated chemical reactivity descriptors.

The HOMO–LUMO energy gap serves as an important indicator of a molecule's kinetic stability. A larger energy gap is typically associated with higher chemical stability, while a smaller HOMO–LUMO gap correlates with increased reactivity. Based on the analysis of the HOMO–LUMO energy gaps, the order of chemical reactivity among the synthesized quinazolin-12-one derivatives (**3a**–**l**) is as follows: **3f** > **3e** > **3d** > **3l** > **3k** > **3j** > **3i** > **3h** > **3g** > **3c** > **3b** > **3a**. Notably, compound (**3f**) possesses the lowest HOMO–LUMO energy gap, indicating that it is the most reactive among the synthesized molecules. Additionally, hardness (η) and softness (S) are significant descriptors of a molecule's behavior during chemical reactions. Generally, hard molecules exhibit high resistance to changes in their electronic distribution during a reaction, whereas soft molecules show low resistance to such changes. The results reveal that compound (**3f**) demonstrates high softness, indicating its low resistance to alterations in electronic distribution during reactions. Furthermore, electronegativity, defined as an atom's tendency to attract electrons within a chemical bond, plays a crucial role in determining the stability and strength of molecular interactions. Conversely, electrophilicity refers to the ability of a species to accept electrons, making it a critical factor in nucleophilic attack mechanisms. Among the synthesized compounds, compound

(**3c**) exhibits higher electronegativity and electrophilicity, thereby enhancing its potential for biological interactions.

Molecular docking studies

Molecular docking is a computational technique used to predict the optimal orientation and binding affinity of a ligand to a receptor when they form a stable complex. This method is essential for elucidating the molecular interactions that play a role in various biological processes, including signal transduction, enzyme catalysis, and pharmacological activity. The significance of molecular docking lies in its ability to simulate and forecast the binding affinity and orientation of ligands within the active sites of target proteins. Such predictions are critical for understanding the molecular mechanisms that govern biological functions, including enzyme inhibition, signal transduction, and receptor activation. By accurately modeling these interactions, researchers can identify promising drug candidates and refine their binding characteristics to improve therapeutic efficacy while minimizing adverse effects.^{31,32} In this study, we focused on PDK1, utilizing its crystallographic structure resolved at 2.70 Å obtained from the Protein Data Bank (PDB) ID 2R7B.³³ The amino acid residues required for the catalytic site were identified, and a docking protocol was established to predict bioactive conformations. As demonstrated in Fig. 4, the root mean square deviation (RMSD) between the original ligand and the re-docked ligand was quantified at 0.38 Å, confirming the reliability of the docking protocol.^{27a}

Fig. 5 illustrates that all the quinazolin-12-one derivatives (**3a**–**l**) under investigation interacted with the same binding site as the native compound. To determine the binding affinities and scores of the derivatives, the interactions between the synthesized compounds and the amino acid residues in the active site were examined.

All of the derivatives had excellent binding scores and impressive binding affinities, according to the provided results. The binding energy of compound (**3f**) was found to be the most favorable, at $-10.44 \text{ kcal mol}^{-1}$. The best configuration of compound (**3f**) was selected, and subsequently, a comprehensive analysis of both bonding and non-bonding interactions was performed. Table 4 presents the interactions and docking results for the synthesized derivatives. The amino acid residues involved in both bonding and non-bonding interactions with compound (**3f**) include Ala162, Leu212, Val96, Leu88, Ala109,



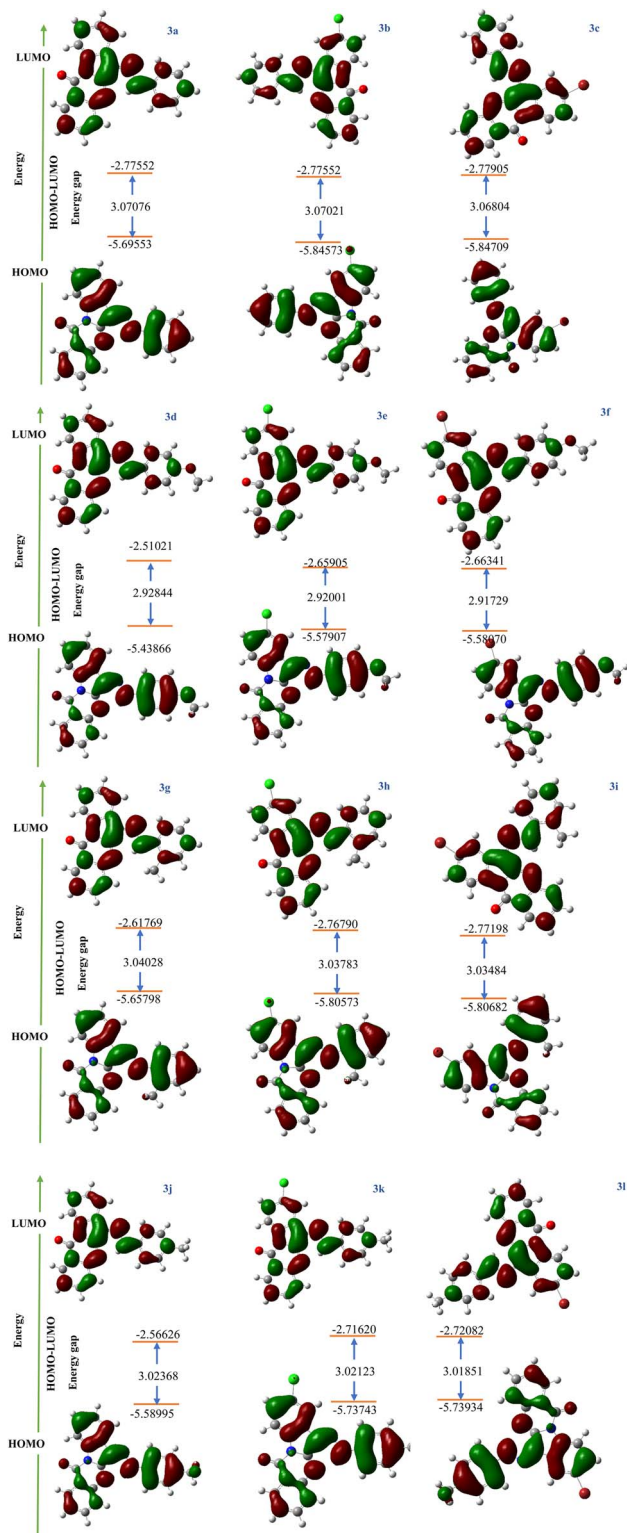


Fig. 3 FMOs for the synthesized derivatives (3a–l).

Glu209, Thr222, Lys207, Asn210, Asp223, Lys86, Lys163, Gly165, Tyr161, Ser160, Val143, Leu159, Lys111, Glu166, Gly89, Gly91, Asn164, Lys169, and Glu90.

Compound (3f) exhibits the highest binding energy of $-10.44 \text{ kcal mol}^{-1}$ among the synthesized derivatives,

indicating a strong affinity for the target protein PDK1. This notable binding affinity is significant because PDK1 is involved in various signaling pathways, and effective inhibition may yield substantial therapeutic benefits, particularly in the context of cancer and metabolic disorders. In contrast, compounds (3a) and (3b) display similar binding energies of -10.10 and $-10.23 \text{ kcal mol}^{-1}$, respectively, but exhibit fewer significant interactions with PDK1. This observation underscores the importance of diverse interactions in enhancing binding affinity. Specifically, compound (3f) establishes critical hydrogen bonds with residues Asn210 and Ala162, thereby stabilizing its binding conformation and augmenting binding affinity through electrostatic interactions. These interactions not only improve the binding profile but also suggest that compound (3f) could effectively inhibit PDK1 activity due to its strong association with key amino acid residues. In comparison, compounds (3c) and (3d) possess binding energies of -10.10 and $-10.04 \text{ kcal mol}^{-1}$, respectively, but they lack the extensive hydrophobic interactions present in compound (3f) with residues such as Val96 and Leu212. Hydrophobic interactions are essential as they increase the contact area between the ligand and protein, promoting a more energetically favorable configuration. This deficiency likely accounts for the lower binding affinities of compounds (3c) and (3d). Moreover, compounds (3e) and (3g) exhibit binding energies of -10.40 and $-10.35 \text{ kcal mol}^{-1}$, respectively, but similarly lack the interaction diversity characteristic of compound (3f). The combination of various interactions, including π - π stacking and van der Waals forces, further stabilizes compound (3f) within the binding pocket. Notably, π - π stacking significantly contributes to the strength and specificity of the interaction, while van der Waals forces optimize the spatial arrangement within the active site, thus enhancing the likelihood of effective inhibition. Conversely, compounds (3h) through (3l) demonstrate lower binding energies and fewer critical interactions, indicating a correlation between the diversity of interactions and binding affinity. This finding highlights the necessity of a multifaceted interaction profile for achieving greater binding potency, emphasizing that compounds with richer interaction landscapes can provide more effective inhibition. The superior binding affinity of compound (3f) underscores its potential as a potent PDK1 inhibitor, which may lead to important advancements in therapeutic strategies targeting PDK1-related diseases. The native ligand exhibited substantial bonding and non-bonding interactions with the target protein. Through important interactions, the amino acid residues Lys111, Val96, Leu88, Asp223, Thr222, Ser160, Ala162, Lys163, Gly165, Glu166, Asn164, Lys86, Gly89, Leu159, Val143, and Tyr161 greatly contributed to the stability of the protein. The native ligand formed strong hydrogen bonds with Ser160, Asp223, and Thr222, with a docking score of $-9.99 \text{ kcal mol}^{-1}$. On the other hand, BX-517 was evaluated as the standard compound with the synthesized compounds. The results indicated that this compound, with a docking score of $-8.49 \text{ kcal mol}^{-1}$, can form three key hydrogen bonds with the amino acids Leu88, Ser160, and Thr222. These residues overlap with some of the critical interactions observed for the native ligand, which also forms

Table 3 Energetic parameters of the compounds (3a–l)

Compound	E_{HOMO} (eV)	E_{LUMO} (eV)	ΔE_{gap}	Hardness (η) (eV)	Softness (S) (eV)	Electronegativity(χ) (eV)	Electrophilicity (ψ)
3a	−5.6955	−2.6247	3.0707	1.5353	0.3256	4.1601	5.6360
3b	−5.8457	−2.7755	3.0702	1.5351	0.3257	4.3106	6.0521
3c	−5.8470	−2.7790	3.0680	1.5340	0.3259	4.3130	6.0633
3d	−5.4386	−2.5102	2.9284	1.4642	0.3414	3.9744	5.3940
3e	−5.5790	−2.6590	2.9200	1.4600	0.3424	4.1190	5.8104
3f	−5.5807	−2.6634	2.9172	1.4586	0.3427	4.1220	5.8243
3g	−5.6579	−2.6176	3.0402	1.5201	0.3289	4.1378	5.6316
3h	−5.8057	−2.7679	3.0378	1.5189	0.3291	4.2868	6.0493
3i	−5.8068	−2.7719	3.0348	1.5174	0.3295	4.2894	6.0625
3j	−5.5899	−2.5662	3.0236	1.5118	0.3307	4.0781	5.5002
3k	−5.7374	−2.7162	3.0212	1.5106	0.3309	4.2268	5.9134
3l	−5.7393	−2.7208	3.0185	1.5092	0.3312	4.2300	5.9279

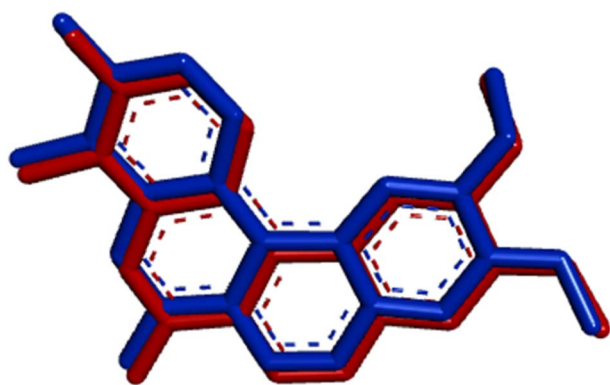


Fig. 4 The superimposition of the native ligand (red) and the docked ligand (blue) illustrates the spatial alignment between these two structures, with an RMSD of 0.38 Å.

strong hydrogen bonds. Additionally, π -alkyl hydrophobic interactions were observed with the amino acids Val96, Ala109, Ala162, Leu212, and Leu88, and an alkyl interaction was identified with the amino acid Val96. While BX-517 demonstrates significant interactions, its lower binding energy compared to the synthesized compounds (3a–l) suggests that it may not achieve the same level of inhibition due to a less diverse interaction profile. Fig. 6, 7, and 8 illustrate the detailed 2D and 3D binding interactions of compound (3f), the native ligand, and BX-517 within the active site of PDK1. Gaining a comprehensive understanding of these interactions could provide critical insights for the development of new inhibitors that leverage similar binding mechanisms, thereby improving therapeutic efficacy and selectivity in forthcoming drug development initiatives. Such knowledge can directly guide medicinal chemistry endeavors focused on the creation of optimized compounds targeting PDK1.

MD simulation

RMSD serves as a pivotal tool for elucidating conformational changes and intermolecular interactions, providing critical insights into molecular behavior across diverse environmental

conditions. Such information significantly enhances our understanding of underlying biological mechanisms and contributes to the predictive modeling of molecular performance in pharmaceutical and biological contexts. An MD simulation of 100 ns was carried out for the (3f)–2R7B complex, as shown in Fig. 9. Initially, during the first 20 ns, both the protein and ligand exhibit considerable fluctuations in their RMSD values, with the protein reaching a peak of approximately 2.5 Å and the ligand peaking around 6 Å. These fluctuations indicate that both components undergo substantial conformational adjustments as they interact, which is critical for establishing stable binding interactions. As the simulation progresses into the 20 to 60 ns range, the RMSD values begin to stabilize, particularly for the protein, which fluctuates around 2 Å. This stabilization suggests that the protein has adapted to the ligand's presence, achieving a more defined conformation essential for maintaining its functional integrity. In contrast, the ligand continues to exhibit erratic behavior, oscillating between 4 and 7 Å, indicating that it is still optimizing its binding pose within the protein's active site. This ongoing adjustment is crucial for enhancing the stability of the protein–ligand complex. In the final phase of the simulation, from 60 to 100 ns, the protein RMSD remains relatively stable, reinforcing the notion of a well-established interaction with the ligand. However, the ligand's RMSD shows a notable increase, peaking at approximately 9 Å, which may suggest increased mobility or potential dissociation from the binding site.

Unlike RMSD, which measures the overall deviation of a molecule's structure from a reference, root mean square fluctuation (RMSF) provides insights into the fluctuations of individual atoms or residues relative to their average positions throughout the simulation. By calculating the RMSF for each atom, researchers can identify regions of high flexibility and stability within the molecular structure, which is crucial for understanding conformational changes during molecular interactions, such as protein–ligand binding. This analysis reveals how specific residues contribute to the stability and functionality of the biomolecule. Fig. 10 depicts a comprehensive examination of compound (3f)'s interaction with the residues of the 2R7B binding site. The residues shown in green that



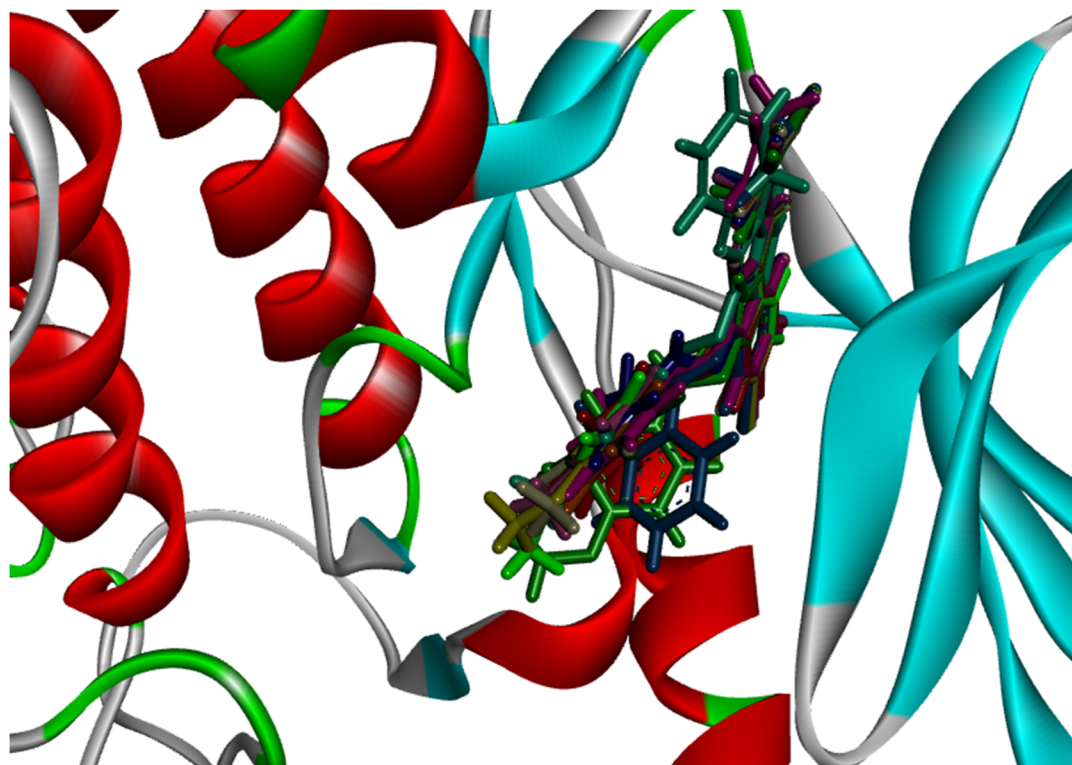


Fig. 5 Superimposed structures of the synthesized derivatives (**3a–l**) in the active site of 2R7B. This depiction highlights the structural diversity of the synthesized compounds and their spatial arrangement within the binding pocket, providing insights into potential interactions with the active site residues.

are involved in this interaction include Lys86, Leu88, Glu90, Gly91, Ser92, Phe93, Ser94, Thr95, Val96, Ala109, Lys111, Tyr126, Arg129, Glu130, Val143, Leu159, Ser160, Tyr161, Ala162, Lys163, Glu166, Lys169, Lys207, Glu209, Asn210, Leu212, Gln220, Thr222, Asp223, Gly225, Thr226, and Gln247. Some of these residues exhibit lower RMSF values, indicating greater stability, which is crucial for maintaining the structural integrity of the protein, particularly in functional domains essential for biological activity. Additionally, the vertical blue bars highlight protein residues, including amino acids Lys120, Ser234, Gly244, and Tyr288, indicating regions of high flexibility. These fluctuations suggest that these residues may undergo significant conformational changes, which could be essential for their roles in biological processes such as ligand binding or protein–protein interactions. The increased mobility in these areas may facilitate necessary adaptations for effective molecular interactions, emphasizing their potential importance in the protein's functionality.

The provided bar chart illustrates the interactions within the (**3f**)–2R7B complex during MD simulations. Fig. 11 categorizes these interactions; each type is represented by a different color, allowing for a clear visual representation of its contributions to the overall binding profile. Residues such as Leu88, Lys111, Ala162, and Asn210 indicate hydrogen bonds with the ligand, which are essential for maintaining the structural integrity of the complex. Among these residues, Ala162 stands out with a notably high interaction fraction, suggesting that it may be

a critical residue for the binding affinity of compound (**3f**). The presence of hydrophobic interactions, represented by the blue bars, further emphasizes the importance of non-polar interactions in stabilizing the protein–ligand complex. Residues like Val96, Ala109, Leu159, Tyr161, and Leu212 contribute to these hydrophobic contacts, which are vital for overall binding affinity. Additionally, the chart highlights the presence of ionic interactions, depicted in pink, and water bridge interactions, shown in purple. Although these interactions are less frequent compared to hydrogen bonds and hydrophobic interactions, they still play a role in the stability of the complex. For example, the ionic interaction involving Lys111 suggests that electrostatic forces may contribute to the binding mechanism, particularly in stabilizing the ligand's position within the binding site. Water bridges, while less prominent, can also facilitate interactions by providing additional stabilization through solvent-mediated contacts.

The study of the entrapment of compounds within targeted amino acid residues provides significant insights into the binding mechanism. As illustrated in Fig. 12, Ala162 remained consistently embedded by compound (**3f**) for over 85% of the simulation duration. Additionally, compound (**3f**) demonstrated sustained interactions with Leu88, Tyr161, and Leu212, remaining buried with these residues for more than half of the predicted trajectory. In contrast, other amino acid residues exhibited a lower degree of entrapment, suggesting that their interactions with the ligand occurred with less frequency. These





Table 4 *In silico* docking results of synthesized compounds (3a–l) against PDK1

Compound	Docking scores	H-bonding	C-bonding	π -donor-H-bonding	π -anion	π -alkyl	π -sigma	Alkyl	van der Waals	Unfavorable
3a	−10.10	Ala162				Leu212,Val96,Leu88,Ala109			Glu209,Thr222,Lys207,Asn210,Asp223,Lys86,Lys163,Gly165,Tyr161,Ser160,Val143,Leu159,Lys111	Glu166
3b	−10.23	Ala162		Glu166		Ala109,Val96,Leu88,Leu212		Leu159,Lys111,Val96	Glu209,Asn210,Lys207,Lys86,Gly165,Lys163,Tyr161,Ser160,Val143,Thr222,Gly89,Asp223	Glu166
3c	−10.10	Ala162				Ala109,Val96,Leu88,Leu212		Leu159, Lys111	Glu209,Asn210, Asp223, Thr222, Val143, Ser160, Tyr161, Gly165, Lys163, Lys86	Glu166
3d	−10.04	Ala162	Asn210	Thr222	Asp223	Ala109,Val96,Leu88,Leu212			Lys207,Glu209,Lys111,Leu159,Val143,Ser160,Tyr161,Lys163,Gly165,Lys86,Gly91	
3e	−10.40	Ala162			Glu166	Ala109,Val96,Leu88,Leu212		Leu159, Lys111,Val96	Lys207,Glu209,Asn210,Asp223,Thr222,Val143,Ser160,Tyr161,Lys163,Gly165,Lys86,Gly89	Glu166
3f	−10.44	Ala162	Asn210			Val96,Ala109,Leu88,Leu212		Leu159,Lys111	Asp223,Glu209,Lys207,Thr222,Val143,Ser160,Tyr161,Lys163,Ser160,Leu159,Lys111,Thr222	Glu166
3g	−10.35	Ala162				Leu212,Val96,Leu88,Ala109		Leu212	Lys207,Glu209,Asn210,Asp223,Lys86,Lys163,Gly165,Tyr161,Ser160,Val143,Leu159,Lys111,Thr222	Glu166
3h	−10.18	Ala162			Glu166	Ala109,Val96,Leu212,Leu88	Leu88	Leu159,Lys111,Val96,Leu88	Gly89,Thr222,Val143,Ser160,Tyr161,Lys163,Lys86,Asn164,Gly165,Lys169,Asp223,Lys207,Asn210,Glu209	Glu166
3i	−9.99	Ala162				Leu159,Lys111		Ala109,Val96,Leu88,Leu212	Gly91,Gly89,Glu90,Thr222,Val143,Ser160,Tyr161,Gly165,Lys163,Lys86,Asp223,Glu209,Asn210	Glu166
3j	−10.25	Ala162				Leu88,Val96,Ala109,Leu212			Lys207,Glu209,Thr222,Lys111,Leu159,Val143,Ser160,Tyr161,Gly165,Lys163,Lys86,Asp223,Asn210	Glu166
3k	−10.26					Leu88,Ala109,Leu212	Leu88	Val143,Ala109,Leu159	Asn210,Lys207,Glu209,Asp223,Lys169,Lys86,Asn164,Gly165,Lys163,Tyr161,Ser160,Val96,Thr222	Glu166
3l	−10.15	Ala162			Glu166	Ala109,Lys111		Leu159,Val96,Leu88,Leu212	Glu209,Lys207,Asn210,Lys86,Gly165,Lys163,Tyr161,Ser160,Val143,Thr222,Asp223,Gly89	Glu166



Table 4 (Contd.)

Compound	Docking scores	H-bonding	C-bonding	π -donor-H-bonding	π -anion	π -alkyl	π -sigma	Alkyl	van der Waals	Unfavorable
Native ligand	-9.49	Ser160, Asp223, Thr222	Ser160, Ala162, Lys163, Gly165, Leu88, Glu166			Leu88, Lys111, Val96	Leu88	Leu88, Lys111, Val96	Asn164, Lys86, Gly89, Leu159, Val143, Tyr161	
BX-517	-8.49	Leu88, Ser160, Thr222				Val96, Ala109, Ala162, Leu212, Leu88, Val96		Val96	Lys86, Leu166, Gly89, Asp223, Glu90, Lys111, Leu159, Val143, Lys163, Lys163, Tyr161, Gly165	

observations highlight the critical residues involved in the binding process, indicating that certain amino acids play a more prominent role in stabilizing the ligand within the binding pocket. Understanding the dynamics of these interactions aids in elucidating the binding mechanism and can inform the design of more effective compounds targeting specific proteins.

The analysis of structural and dynamic properties of molecules is essential for a comprehensive understanding of their behavior under various conditions. Key tools in this context include the RMSD, which aids in the assessment of stability and structural congruence. The radius of gyration (rGyr) describes the distribution of mass within the molecule, providing insights into its shape and compactness. The solvent-accessible surface area (SASA) quantifies the surface area of the molecule that is accessible to solvent, facilitating the understanding of intermolecular interactions. Intramolecular hydrogen bonds (intraHB) play a crucial role in stabilizing the three-dimensional structures of molecules. Furthermore, the molecular surface area (MolSA) and polar surface area (PSA) characterize the surface properties of the molecule, which significantly influence its biological and chemical interactions. Collectively, these parameters serve as vital tools for analyzing and predicting molecular behavior in MD simulations. Fig. 13 presents a comprehensive overview of these properties for the (3f)-2R7B complex. The RMSD and rGyr values were observed to fall within the ranges of 0.4 to 2.3 Å and 4.1 to 4.9 Å, respectively. Additionally, the presence of intraHB was recorded within the range of 0 to 1 at specific intervals during the simulation. The MolSA exhibited variability between 342 and 372 Å², while the SASA ranged from 10 to 400 Å², and the PSA was found to fluctuate between 5 and 100 Å².

The torsional degree of freedom refers to the rotation occurring around a single bond within a molecule, allowing the molecule to adopt an optimal conformation for protein interaction. Torsional degree values were calculated for the (3f)-2R7B complex. The trajectory simulation identified fluctuations in certain bonds within compound (3f). As depicted in Fig. 14a, during this simulation, C-N, N-N, and C-O bonds exhibited modifications in their torsional conformations. Notably, the bonds between atoms 14 and 27, as well as those between atoms 9 and 20, displayed three distinct conformations. This suggests the adoption of a unique conformation by kaempferol within the binding pocket of 2R7B. Furthermore, Fig. 14b demonstrates that the potential differences between atoms 14 and 27, and between 9 and 20, were recorded at 7.83 and 7.00 units, respectively. In contrast, the potential differences for the bonds between atoms 19 and 20, and between 19 and 15, were measured at 0.00 units.

Drug-likeness prediction

The physicochemical properties of quinazolin-12-one derivatives (3a-I) were assessed based on established drug-likeness criteria. Various rules have been developed to evaluate the drug-like characteristics of compounds, aiding in the identification and optimization of drug candidates. Lipinski's "RO5"

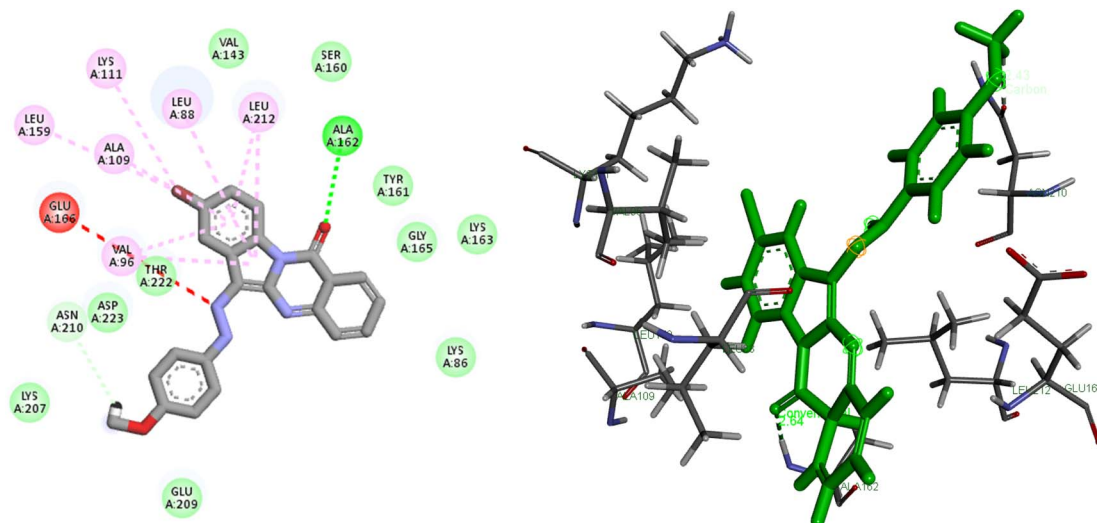


Fig. 6 2D and 3D binding interactions of compound (3f) with the targeted PDK1 (PDB: 2R7B). The figure illustrates key interactions between (3f) and specific amino acids in the binding site, highlighting important hydrogen bonds and hydrophobic interactions that stabilize the ligand–receptor complex.

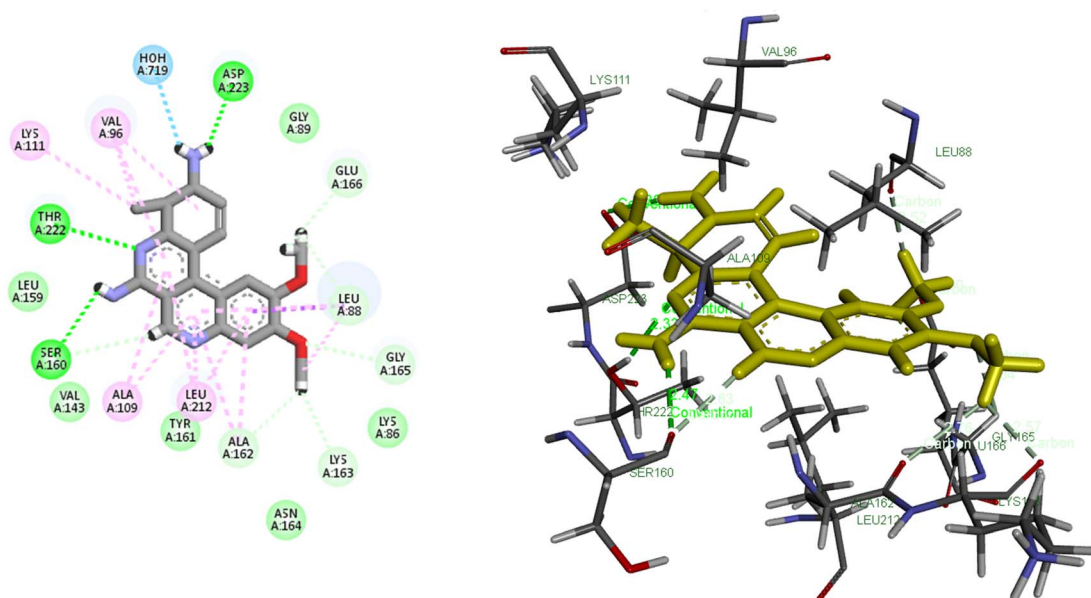


Fig. 7 2D and 3D binding interactions of the native ligand with the targeted PDK1 are shown. Notable interactions include Ser160, Asp223, and Thr222, which contribute to the stability and affinity of the ligand–receptor complex.

specifies four key criteria for oral bioavailability: a molecular weight below 500 daltons, no more than five hydrogen bond donors, no more than ten hydrogen bond acceptors (HBAs), and a log *P* value below five. Ghose's rule defines specific ranges for molecular weight, log *P*, and the number of nitrogen and oxygen atoms to further analyze physicochemical properties. Veber's rule emphasizes the significance of rotatable bonds and hydrogen bonds, suggesting better absorption for compounds with a maximum of ten hydrogen bond donors (HBDs) and acceptors and no more than four rotatable bonds.³⁴ Egan's rule outlines criteria based on physicochemical and structural

features for predicting bioavailability. PAINS alerts highlight undesirable structural patterns that may lead to false positives in biological assays. Lastly, Brenk's rules evaluate toxicological properties and potential side effects, guiding researchers to avoid hazardous compounds. Together, these rules are vital in drug design and development, streamlining the drug discovery process. Table 5 indicates that all synthesized compounds (3a–l), similar to the native ligand and BX-517, satisfy all important parameters. Their molecular weights are all below 500 daltons, suggesting good absorption potential. Each compound has an appropriate number of HBAs and HBDs, enhancing their ability



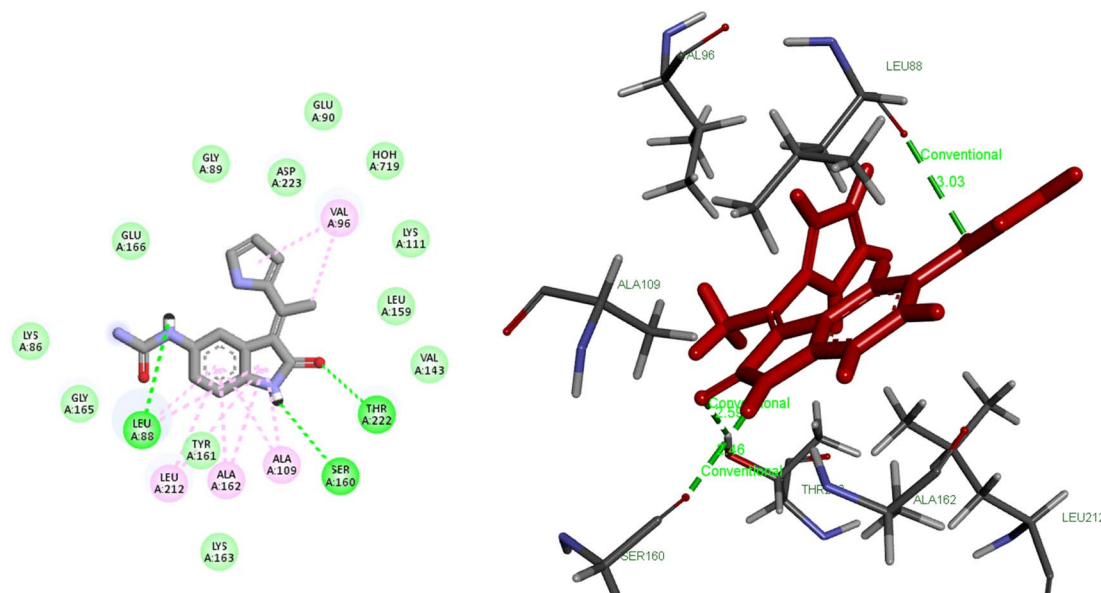


Fig. 8 2D and 3D binding interactions of BX-517 with the targeted PDK1, which have hydrogen bonding interactions with key amino acids, including Leu88, Ser160, and Thr222.

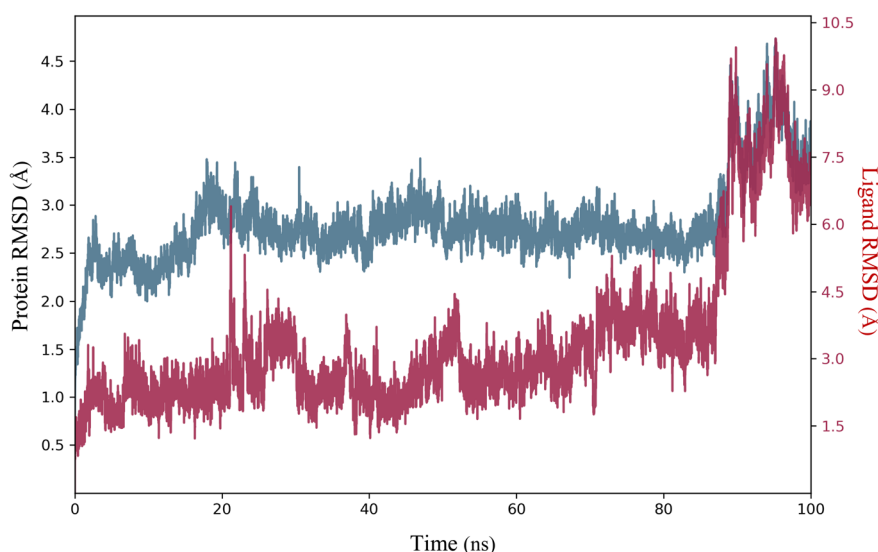


Fig. 9 RMSD values of the (3f)-2R7B complex over a simulation period of 100 ns, indicating the fluctuations in the RMSD of the complex. After 90 ns, the complex achieves stability, as evidenced by the plateau observed in the RMSD values.

to interact with biological targets. The topological polar surface area (TPSA) values are also within suitable limits, indicating improved solubility in water. Additionally, $\log P$ values fall within the optimal range for membrane permeability, balancing hydrophilicity and lipophilicity, which is essential for drug efficacy. All compounds adhere to Lipinski's, Ghose's, and other relevant drug-likeness criteria, indicating favorable profiles and minimal alerts for pan assay interference compounds (PAINS). On the other hand, the synthesized compounds exhibited no alerts according to the Brenk rule, indicating their high safety and stability. In contrast, the native ligand and BX-517 exhibited two and one alerts, respectively, pertaining to aniline, polycyclic

aromatic hydrocarbon-3, and Michael-acceptor-1. This distinction clearly demonstrates that the synthesized compounds outperform the native ligand and BX-517 in this regard, positioning them as safer alternatives in drug design considerations.

In silico ADMET prediction

Drug-likeness findings play a crucial role in ADMET predictions and drug development strategies. By analyzing the physico-chemical properties and structural characteristics of compounds, researchers can more effectively predict their



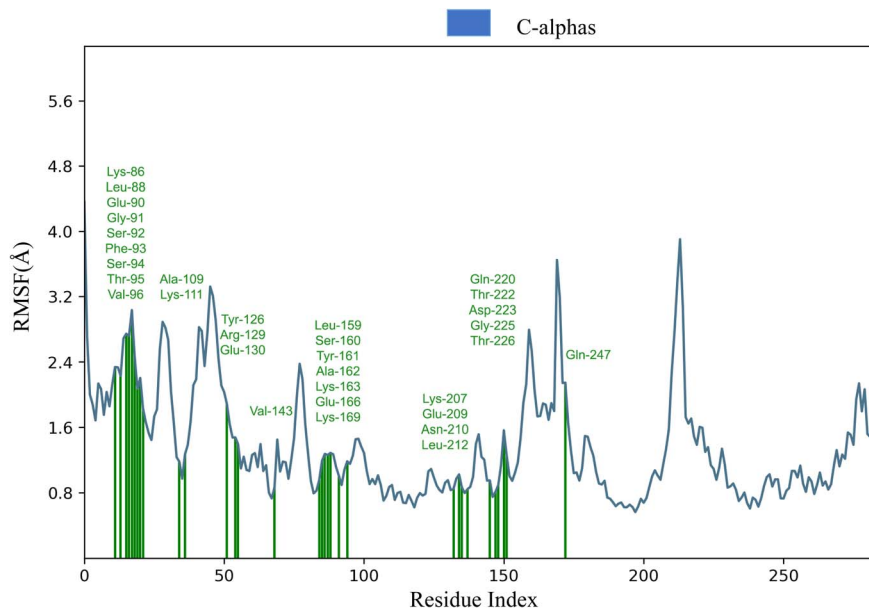


Fig. 10 RMSF plot of the (3f)-2R7B complex, highlighting the amino acids with the greatest fluctuations, indicating their significant flexibility.

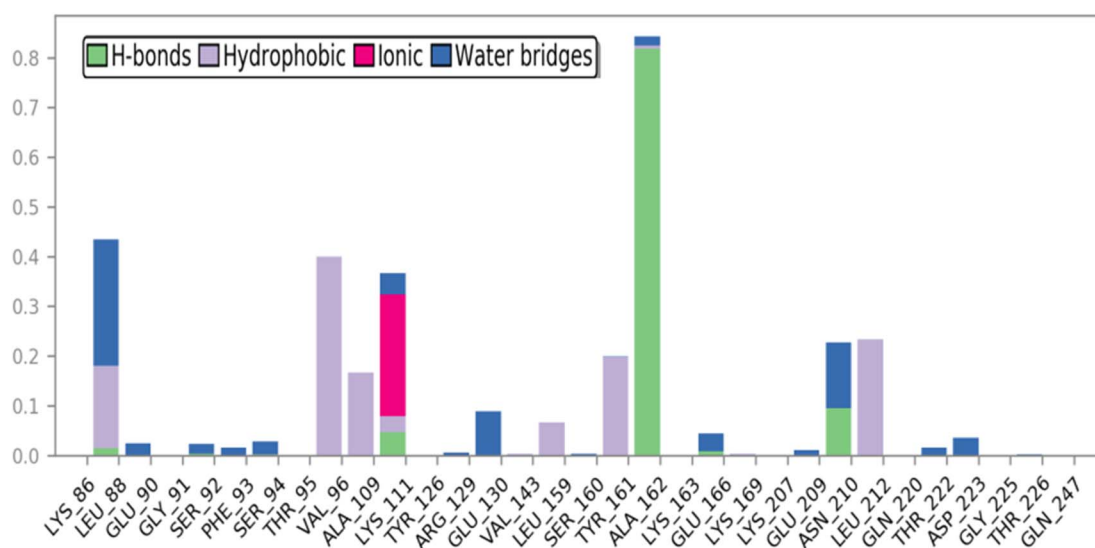


Fig. 11 The (3f)-2R7B interactions during MD simulation, including various types of interactions such as H-bonds (green), hydrophobic interactions (purple), ionic bonds (pink), and water bridges (blue).

behavior in biological systems. Compounds with favorable drug-likeness metrics such as optimal molecular weight, appropriate hydrogen bond counts, and suitable log *P* values are more likely to exhibit effective absorption and distribution. These metrics also assist in selecting lead candidates for further optimization, indicating potential metabolic stability and lower toxicity. Consequently, drug-likeness assessments streamline candidate identification and improve the accuracy of ADMET predictions, leading to more efficient and successful drug development. We conducted *in silico* profiling utilizing ADMETLab³⁵ to evaluate the pharmacokinetic properties of the synthesized compounds (3a-l). Table 6 presents the comprehensive evaluation findings, which reveal encouraging features

across various criteria. The absorption and distribution of pharmaceutical compounds are critical determinants of their therapeutic efficacy and potential side effects. All synthesized compounds, like the native ligand and BX-517, demonstrate effective absorption, enabling them to enter the bloodstream and reach target tissues. All synthesized compounds exhibit high volumes of distribution (VDss), with compound (3f) having the highest VDss at 4.083, indicating extensive tissue distribution and a strong capacity to penetrate the BBB. A higher VDss value is generally advantageous as it signifies better accessibility to tumor tissues, particularly in solid tumors, thereby enhancing the therapeutic efficacy of the compounds. High VDss allows these agents to distribute widely throughout the



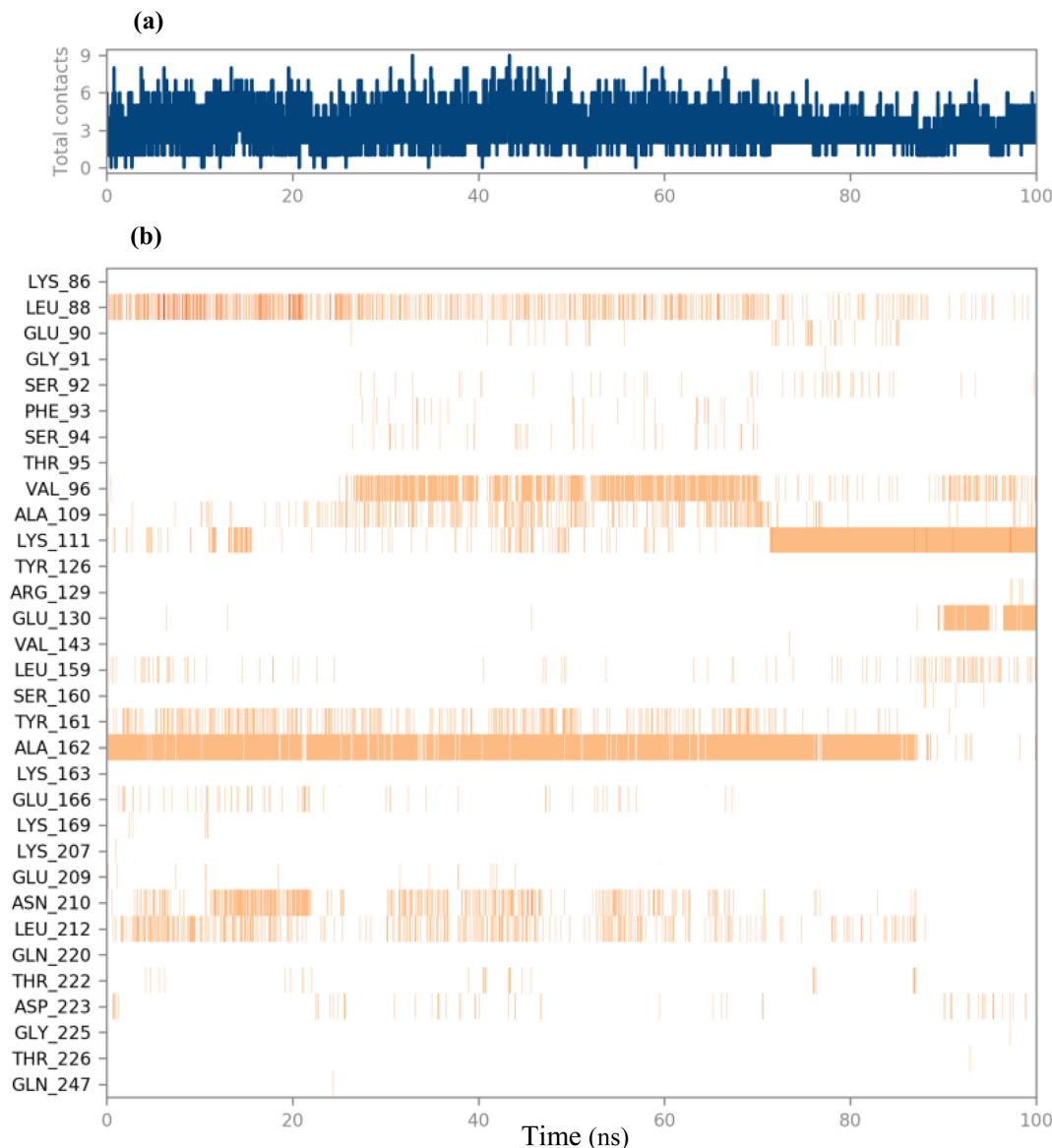


Fig. 12 (a) Timeline depiction showing the total number of molecular interaction contacts for each frame in the trajectory. (b) The number of interactions involving active-site residues for each of the 100 simulated trajectory frames.

body and effectively reach target areas beyond the site of administration. However, potential drawbacks exist for a high VDss. A wide distribution may lead to the accumulation of the drug in non-target tissues, increasing the likelihood of side effects and necessitating higher dosage levels to achieve therapeutic concentrations at the tumor site. In contrast, BX-517 presents the lowest VDss, indicating that it tends to concentrate in plasma, which facilitates easier management and could reduce the risk of adverse effects. Nevertheless, a low VDss may result in insufficient penetration into tumor tissues, potentially diminishing the therapeutic impact and leading to suboptimal treatment outcomes. The ability of a compound to cross the BBB has significant implications for its therapeutic applications and safety profile. Compounds that can penetrate this barrier often have several advantages. For instance, they can effectively

target central nervous system (CNS) disorders such as Alzheimer's disease, Parkinson's disease, and brain tumors. This direct access to the brain translates into potentially higher therapeutic efficacy, as these compounds achieve higher concentrations in brain tissue, thereby enhancing treatment outcomes. Furthermore, by delivering medications directly to the CNS, there is a possibility to minimize systemic side effects, reducing the likelihood of adverse effects in other parts of the body. However, the capacity to cross the BBB also introduces certain disadvantages. One major concern is the risk of CNS-related side effects that these compounds may cause. These side effects can include sedation, confusion, and in severe cases, neurotoxicity. Chronic exposure to certain CNS-active agents may lead to neurodegenerative changes, complicating treatment protocols. Additionally, compounds that penetrate



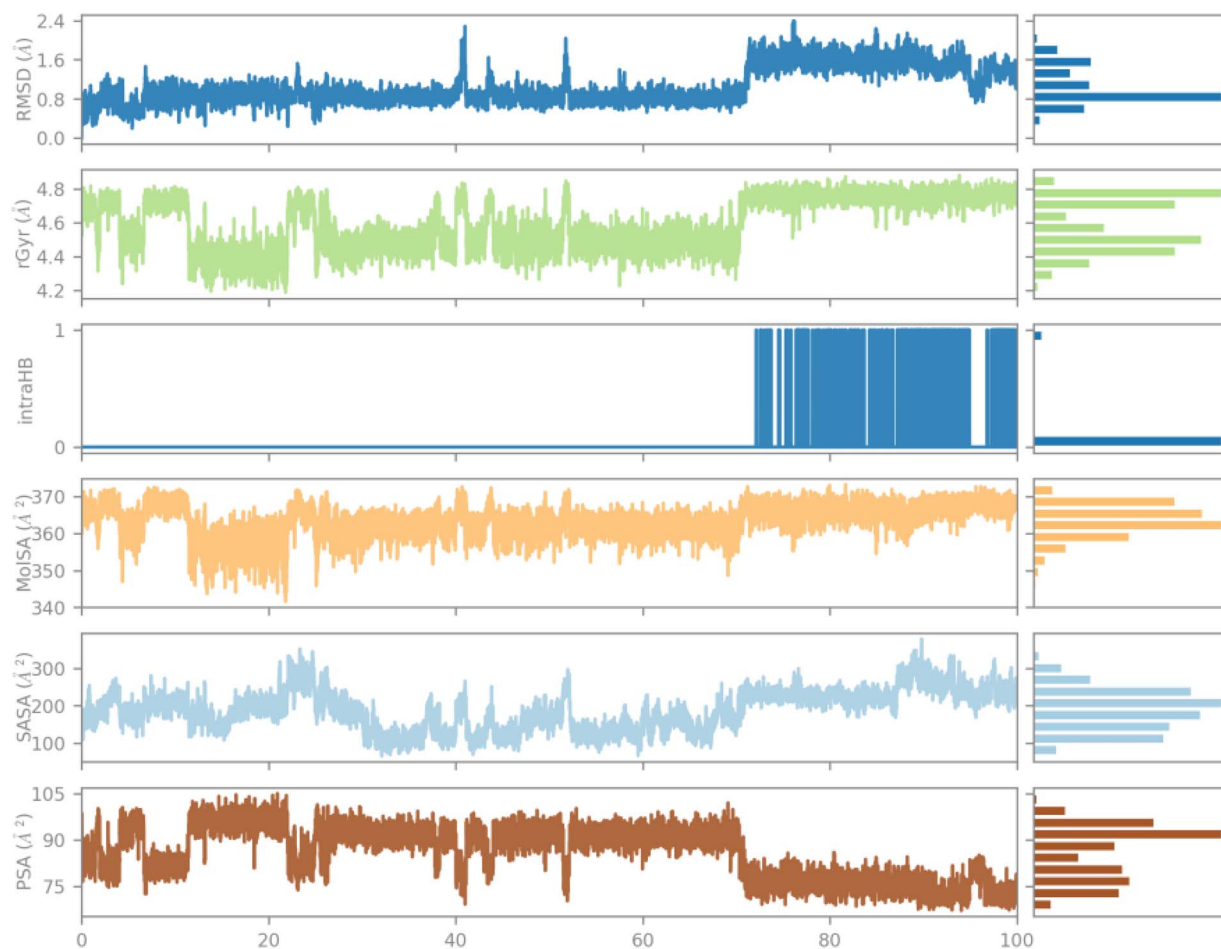


Fig. 13 Time evolution of various structural metrics during the MD simulation of the (3f)–2R7B complex. The plots illustrate RMSD, rGyr, intraHB, MoSAA, SASA, and PSA across 100 trajectory frames.

the BBB may interact with other CNS-active drugs, resulting in unexpected pharmacological effects or diminishing the efficacy of concurrent therapies. All synthesized compounds, such as native ligands and BX-517, possess the ability to effectively cross the BBB, allowing them to target CNS disorders. Compounds with high plasma protein binding (PPB) typically bind strongly to plasma proteins, which can decrease the free drug concentration in circulation, thereby reducing side effects while potentially compromising overall efficacy. Conversely, compounds with low PPB binding may lead to increased free concentrations in the bloodstream, resulting in higher systemic exposure and an elevated risk of adverse effects. Overall, the synthesized compounds (3a–l) differentiate themselves from BX-517 and the native ligand by exhibiting low PPB, which allows for greater availability of free drug in the system. The evaluation of the metabolic activity of the synthesized compounds, in contrast to BX-517, which exhibits a positive effect, showed no impact on CYP2D6. However, significant activity was observed against CYP3A4, CYP1A2, and CYP2C19. This indicates that these compounds can effectively participate in metabolic processes, particularly with CYP3A4, which metabolizes about 50% of all drugs. Such activity raises

concerns about potential drug–drug interactions, as co-administration with other drugs that are substrates of these enzymes may alter plasma concentrations, increasing the risk of toxicity or reducing therapeutic efficacy. Moreover, the activity against CYP1A2 and CYP2C19 underscores the importance of careful monitoring when these compounds are used alongside drugs metabolized by these enzymes. While the compounds demonstrate promising metabolic properties, a deeper understanding of their interactions with specific CYP enzymes is crucial for optimizing their therapeutic use and ensuring patient safety. The importance of drug toxicology lies in its critical role in ensuring the safety and efficacy of pharmaceutical compounds. By systematically evaluating the adverse effects of drugs on biological systems, drug toxicology helps identify potential risks associated with drug exposure, including toxicity, side effects, and interactions. This knowledge is essential for guiding the drug development process, as it informs researchers about the safety profiles of new therapeutics. Ultimately, a thorough understanding of drug toxicology is essential for ensuring that medications are both effective and safe for widespread use. The toxicity analysis of the synthesized compounds, the native ligand, and BX-517 reveals their safety



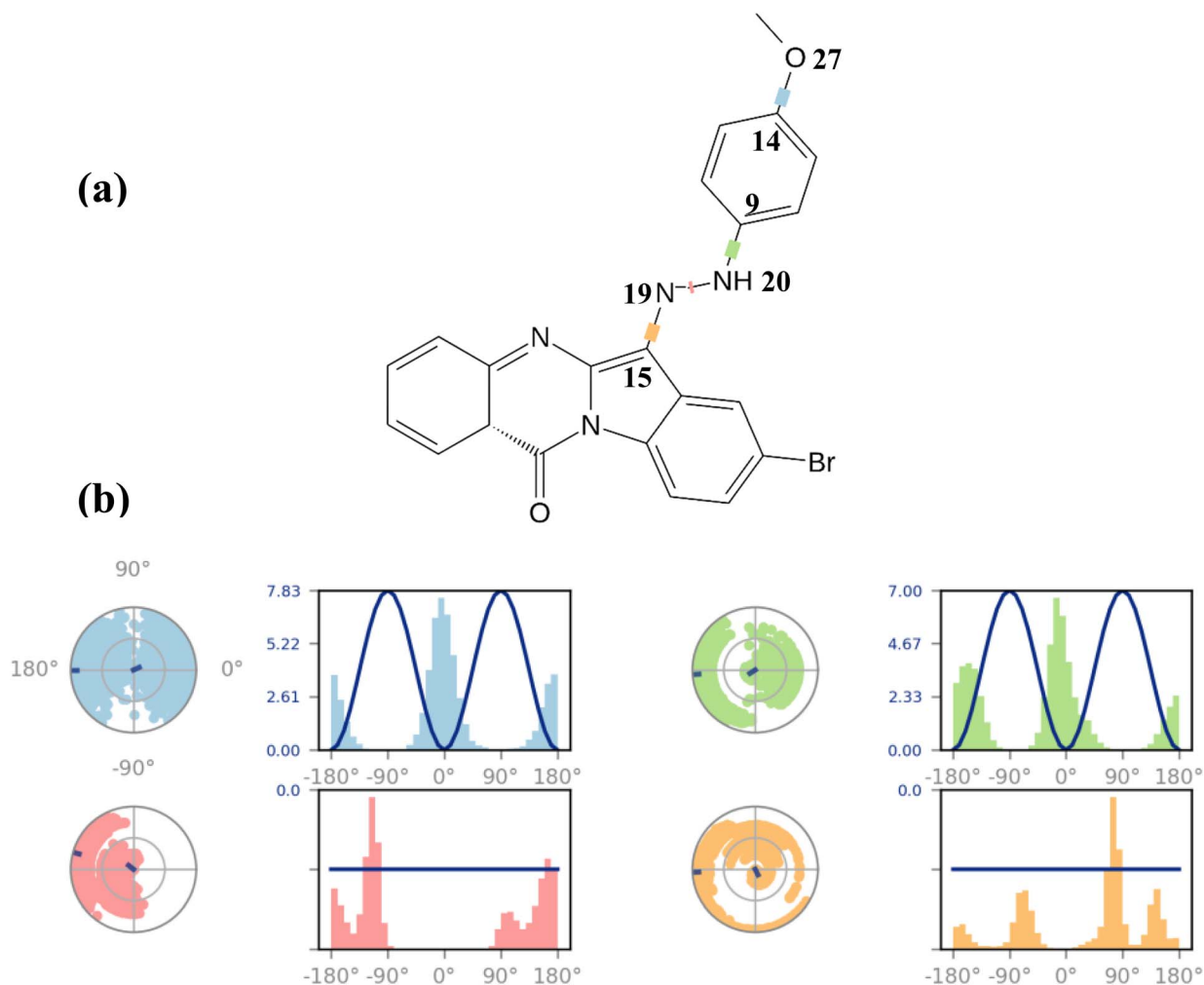


Fig. 14 (a) 2D schematic of compound (3f) with different color-coded rotatable bonds. (b) Torsional analysis of compound (3f) conformations.

Table 5 Pharmacokinetic properties of the compounds (3a–l)

Compound	MW (g mol ⁻¹)	HBA	HBD	TPSA	MLog	P	MR	nRot	Lipinski	Ghose	Veber's rule	Egan	PAINS (alert)	Brenk
3a	338.36	2	2	61.66	3.57	115.34	1	+	+	+	+	+	0	0
3b	372.81	2	2	61.66	4.06	115.34	1	+	+	+	+	+	0	0
3c	417.26	2	2	61.66	4.17	118.03	2	+	+	+	+	+	0	0
3d	368.39	3	2	70.89	3.25	116.82	1	+	+	+	+	+	0	0
3e	402.83	3	2	70.89	3.73	121.83	2	+	+	+	+	+	0	0
3f	447.28	3	2	70.89	3.84	124.52	1	+	+	+	+	+	0	0
3g	352.39	2	2	61.66	3.79	115.30	1	+	+	+	+	+	0	0
3h	386.83	2	2	61.66	4.28	120.31	1	+	+	+	+	+	0	0
3i	431.28	2	2	61.66	4.38	123.00	1	+	+	+	+	+	0	0
3j	352.39	2	2	61.66	3.79	115.30	1	+	+	+	+	+	0	0
3k	386.83	2	2	61.66	4.28	120.31	1	+	+	+	+	+	0	0
3l	431.28	2	2	61.66	4.38	123.00	1	+	+	+	+	+	0	0
Native ligand	334.37	4	2	96.28	1.80	101.31	2	+	+	+	+	+	0	2 ^a
BX-517	282.30	3	4	100.01	0.87	83.90	3	+	+	+	+	+	0	1 ^b

^a Alerts: aniline, polycyclic_aromatic_hydrocarbon_3. ^b Michael_acceptor_1.

profiles. Most synthesized compounds (3a–l) are categorized as either toxic or non-toxic. This ambiguity complicates their development and clinical safety evaluations. In contrast,

compounds 3d and 3g are distinctly safer, similar to the native ligand and BX-517, as they are classified as 'negative' for Ames toxicity. Regarding hepatotoxicity, none of the synthesized





Table 6 ADMET profile of compounds (3a–l)^a

Compound	Absorption		Distribution		Metabolism				Excretion				Toxicity				
	Human intestinal absorption	VDss	BBB permeability	PPB permeability	Substrate		Inhibitors		Total clearance	Ames toxicity	Hepatotoxicity						
					Categorical (Yes/no)	Numeric (L kg ⁻¹)	Categorical (Yes/no)	Numeric (mL min ⁻¹ kg ⁻¹)									
3a	Yes	1.057	Yes	No	2D6	3A4	1A2	2C19	2C9	2D6	3A4	2.33	Yello	No			
3b	Yes	0.857	Yes	No	0.000	---	+++0.998	+++0.967	+++0.999	---	+++0.914	2.17	Yello	No			
3c	Yes	2.221	Yes	No	---	-0.007	+++0.995	+++0.988	+++0.999	---	+++0.782	1.95	Yello	No			
3d	Yes	2.055	Yes	No	+++0.431	---	+++0.988	+++0.994	+++0.994	---	+++0.864	3.69	No	No			
3e	Yes	1.863	Yes	No	+0.635	---	+++0.990	+++0.992	+++0.996	---	+++0.901	1.95	Yello	No			
3f	Yes	4.083	Yes	No	+++0.901	---	+++0.970	+++0.994	+++0.996	---	+++0.882	1.95	Yello	No			
3g	Yes	1.228	Yes	No	---	-0.040	+++0.991	+++0.999	+++0.999	-0.028	+++0.705	3.24	No	No			
3h	Yes	1.127	Yes	No	---	-0.0134	+++0.992	+++0.998	+++0.999	-0.200	+++0.826	3.13	Yello	No			
3i	Yes	2.146	Yes	No	---	-0.051	+++0.978	+++0.998	+++0.999	---	+++0.707	3.01	Yello	No			
3j	Yes	1.813	Yes	No	-0.223	-0.116	+++0.999	+++0.999	+++0.999	---	+++0.982	2.53	No	No			
3k	Yes	1.562	Yes	No	---	-0.068	+++0.999	+++0.998	+++0.999	---	+++0.989	2.27	Yello	No			
3l	Yes	3.462	Yes	No	-0.234	-0.159	+++0.998	+++0.999	+++0.999	---	+++0.982	2.19	Yello	No			
Native ligand	Yes	2.208	Yes	Yes	+++0.836	+++0.897	+++0.961	+0.665	-0.152	---	+++0.997	5.71	No	No			
BX-517	Yes	1.389	Yes	Yes	---	-0.00	-0.375	-0.171	---	-0.005	+++0.724	---	-0.000	-0.979	4.78	No	No

^a Yellow: between yes and no.

compounds exhibit hepatotoxic effects, similar to the native ligand and BX-517. This distinction highlights the synthesized compounds as safer alternatives for therapeutic use.

Conclusion

The molecular docking results revealed that all synthesized compounds exhibited superior binding affinities toward the PDK1 enzyme compared to the native ligand and BX-517, which served as standard compounds. Among these, compound (**3f**) demonstrated the highest binding affinity, achieving a docking score of $-10.44 \text{ kcal mol}^{-1}$. RMSD analysis confirmed that compound (**3f**) consistently formed stable interactions with key residues of PDK1, affirming the thermodynamic stability of the (**3f**)–PDK1 complex throughout the 100 ns simulation trajectory. Additionally, DFT analysis indicated a high level of chemical reactivity for all molecules. Notably, compound (**3f**) exhibited the smallest HOMO–LUMO energy gap, underscoring its stability and enhanced biological activity. ADME property analysis further showed that all compounds, similar to the native ligand and BX-517, possessed favorable pharmacological profiles. None of the synthesized molecules violated Lipinski's RO5 or other essential drug-likeness criteria, such as the Ghose, Veber, and Eggan rules. These analyses confirm that the compounds exhibit good human intestinal absorption and have a high VDss, with compound (**3f**) achieving the highest VDss value of 4.083. This indicates extensive tissue distribution and a strong capacity to penetrate the BBB. Overall, the synthesized compounds (**3a–l**) differentiate themselves from BX-517 and the native ligand by exhibiting low PPB, which enhances the availability of free drug within the system. Investigation of both *in vivo* and *in vitro* models may provide valuable insights and recommendations for future research directions.

Experimental

General

The solvents and reagents used in this study were of synthetic grade and were supplied by Aldrich and Merck. Melting points were measured using an electro-thermal 9100. FT-IR spectra were recorded using KBr disks on a Bruker Tensor 27 spectrometer, with absorbance values reported in cm^{-1} . NMR spectra were recorded on a Bruker DRX-300 Avance instrument in ppm (300 MHz for ^1H and 75.4 MHz for ^{13}C), using $\text{DMSO-}d_6$ as the solvent and TMS as the internal standard. Mass spectra were recorded using an Agilent Technologies 5975C VL MSD with a triple-axis detector, operating at 70 eV using the EI method.

General procedure for synthesizing quinazolin-12-one derivatives (**3a–l**)

A mixture of tryptanthrins (**1a–c**) (1 mmol) and phenylhydrazine hydrochloride (**2a–d**) (1 mmol) was heated to reflux in CH_3CN (5 mL), which served as the solvent. After an appropriate reaction time, orange precipitates were observed. The completion of the reaction and the formation of compounds (**3a–l**) were

confirmed by thin layer chromatography (TLC) using a solvent system of ethyl acetate/*n*-hexane (1 : 1). The solid products were subsequently filtered and washed with ethanol, resulting in the isolation of pure products.

6-(Phenyl-hydrazono)-6*H*-indolo[2,1-*b*]quinazolin-12-one (**3a**)

Orange solid, M.p.: 260–262 °C, yield: 0.285 g (84%); IR (KBr) ($\nu_{\text{max}} \text{ cm}^{-1}$): 3100 (NH), 3035 (=CH), 1678 (C=O), 1599, 1544 (C=C), 1466 (C–N), 1315 (C–NH), 1249, 1174 (C–N), 755 (Ar). ^1H NMR (300 MHz, $\text{DMSO-}d_6$): δ 13.49 (1H, s, NH), 8.58 (1H, d, $^3J = 6.0 \text{ Hz}$, ArH), 8.46 (1H, d, $^3J = 6.0 \text{ Hz}$, ArH), 7.88 (1H, d, $^3J = 6.0 \text{ Hz}$, ArH), 7.81 (2H, d, $^3J = 3.0 \text{ Hz}$, ArH), 7.55 (1H, m, ArH), 7.38–7.49 (6H, m, ArH), 7.11 (1H, t, $^3J = 6.0 \text{ Hz}$, ArH). ^{13}C NMR (75 MHz, $\text{DMSO-}d_6$): δ 158.5 (C=O), 146.7 (N=C–N), 148.5 (C=N), 142.6 (C–NH), 142.5, 136.9 (2N=C=), 134.1, 129.4 (2CH Ar), 128.4, 127.3, 127.2, 127.1, 126.3, 124.3, 123.4, 121.2, 118.9, 116.8 (Ar), 114.5 (2CH Ar).

8-Chloro-6-(phenyl-hydrazono)-6*H*-indolo[2,1-*b*]quinazolin-12-one (**3b**)

Orange solid, M.p.: 270–272 °C, yield: 0.344 g (92%); IR (KBr) ($\nu_{\text{max}} \text{ cm}^{-1}$): 3100 (NH), 3039 (=CH), 1691 (C=O), 1602, 1550 (C=C), 1457 (C–N), 1313 (C–NH), 1258, 1181 (C–N), 745 (Ar), 687 (Cl–C). ^1H NMR (300 MHz, $\text{DMSO-}d_6$): δ 13.40 (1H, s, NH), 8.44 (1H, d, $^3J = 9.0 \text{ Hz}$, ArH), 8.39 (1H, d, $^3J = 9.0$), 7.82–7.73 (3H, m, ArH), 7.52 (1H, t, $^3J = 6.0 \text{ Hz}$, ArH), 7.42–7.38 (4H, m, ArH), 7.33 (1H, d, $^3J = 6.0 \text{ Hz}$, ArH), 7.15–7.10 (1H, m, ArH). ^{13}C NMR (75 MHz, $\text{DMSO-}d_6$): δ 158.4 (C=O), 146.6 (N=C–N), 145.7 (C=N), 142.3 (C–NH), 135.1, 134.4 (2N=C=), 132.1, 129.5 (2CH Ar), 127.9, 127.4, 127.3, 126.1, 125, 124, 121, 118.9, 119, 117.9 (Ar), 114.7 (2CH Ar). MS (EI): m/z (%) = 374 (M+2, 6), 339 (0.5), 343 (4), 267 (27), 239 (3), 207 (19), 177 (5), 97 (8), 80 (98), 64 (100), 48 (84).

8-Bromo-6-(phenyl-hydrazono)-6*H*-indolo[2,1-*b*]quinazolin-12-one (**3c**)

Orange solid, M.p.: 281–284 °C, yield: 0.370 g (88%); IR (KBr) ($\nu_{\text{max}} \text{ cm}^{-1}$): 3100 (NH), 3028 (=CH), 1677 (C=O), 1603, 1547 (C=C), 1458 (C–N), 1314 (C–NH), 1259, 1181 (C–N), 749 (Ar), 688 (Cl–C). ^1H NMR (300 MHz, $\text{DMSO-}d_6$): δ 13.45 (1H, s, NH), 8.42 (1H, d, $^3J = 9.0 \text{ Hz}$, ArH), 8.34 (1H, d, $^3J = 6.0$), 7.91 (1H, d, $^3J = 9.0 \text{ Hz}$, ArH), 7.81–7.72 (2H, m, ArH), 7.56–7.49 (2H, m, ArH), 7.45–7.34 (4H, m, ArH), 7.16–7.06 (1H, m, ArH). MS (EI): m/z (%) = 509 (0.3), 418 (M+1, 70), 389 (16), 361 (5), 338 (3), 311 (100), 281 (13), 252 (2), 233 (22), 204 (52), 177 (34), 154 (9), 133 (52), 102 (15), 77 (99), 48 (51).

6-[(4-Methoxy-phenyl)-hydrazono]-6*H*-indolo[2,1-*b*]quinazolin-12-one (**3d**)

Red solid, M.p.: 242–245 °C, yield: 0.265 g (72%); IR (KBr) ($\nu_{\text{max}} \text{ cm}^{-1}$): 3000 (NH), 2836 (=CH), 1690 (C=O), 1600, 1555 (C=C), 1497 (C–N), 1456 (C–NH), 1238, 1177 (C–N), 1026 (C–O), 763 (Ar). ^1H NMR (300 MHz, $\text{DMSO-}d_6$): δ 13.42 (1H, s, NH), 8.52 (1H, d, $^3J = 9.0 \text{ Hz}$, ArH), 8.40 (1H, d, $^3J = 6.0 \text{ Hz}$, ArH), 7.77 (2H, t, $^3J = 7.5 \text{ Hz}$, ArH), 7.71 (1H, d, $^3J = 7.5 \text{ Hz}$, ArH), 7.49 (1H, t, 3J



= 7.5 Hz, ArH), 7.30–7.40 (4H, m, ArH), 6.93 (2H, d, 3J = 9.0 Hz, ArH), 3.84 (3H, s, OCH₃). ¹³C NMR (75 MHz, DMSO-*d*₆): δ 158.7 (C=O), 156.3 (N=C–N), 146.8 (C=N), 145.8 (C–NH), 136.5, 136.4 (2N=C=), 134.1, 127.7 (2CH Ar), 127.2, 127.1, 126.8, 126.1, 125, 124.6, 121, 118.6, 116.8, 115.7 (Ar), 114.7 (2CH Ar), 55.6 (OCH₃). MS (EI): m/z (%) = 368 (M, 3), 353 (0.8), 325 (0.5), 297 (0.2), 281 (3), 267 (0.7), 251 (1), 233 (1), 207 (12), 191 (2), 176 (0.87), 162 (0.6), 148 (0.5), 133 (18), 119 (3), 96 (4), 80 (100), 64 (81), 48 (88).

8-Chloro-6-[(4-methoxy-phenyl)-hydrazono]-6H-indolo[2,1-*b*]quinazolin-12-one (3e)

Red solid, M.p.: 268–271 °C, yield: 0.340 g (84%); IR (KBr) (ν_{\max} cm^{−1}): 3003 (NH), 2832 (=CH), 1683 (C=O), 1603, 1551 (C=C), 1498 (C–N), 1453 (C–NH), 1241, 1177 (C–N), 1030 (C–O), 766 (Ar), 675 (Cl–C). ¹H NMR (300 MHz, DMSO-*d*₆): δ 13.64 (1H, s, NH), 8.52 (1H, d, 3J = 9.0 Hz, ArH), 8.45 (1H, d, 3J = 6.0 Hz, ArH), 7.84 (3H, t, 3J = 6.0 Hz, ArH), 7.55 (1H, t, 3J = 9.0 Hz, ArH), 7.47 (1H, d, 3J = 9.0 Hz, ArH), 7.37 (2H, d, 3J = 9.0 Hz, ArH), 6.98 (2H, d, 3J = 9.0 Hz, ArH), 3.86 (3H, s, OCH₃).

8-Bromo-6-[(4-methoxy-phenyl)-hydrazono]-6H-indolo[2,1-*b*]quinazolin-12-one (3f)

Red solid, M.p.: 270–272 °C, yield: 0.349 g (78%); IR (KBr) (ν_{\max} cm^{−1}): 3000 (NH), 2830 (=CH), 1683 (C=O), 1604, 1551 (C=C), 1500 (C–N), 1453 (C–NH), 1242, 1172 (C–N), 1032 (C–O), 766 (Ar), 675 (Br–C). ¹H NMR (300 MHz, DMSO-*d*₆): δ 13.56 (1H, s, NH), 8.45 (1H, d, 3J = 6.0 Hz, ArH), 8.42 (1H, d, 3J = 3.0 Hz, ArH), 7.96 (3H, d, 3J = 3.0 Hz, ArH), 7.81 (1H, d, 3J = 3.0 Hz, ArH), 7.49–7.56 (4H, m, ArH), 7.97 (2H, d, 3J = 9.0 Hz, ArH), 3.86 (3H, s, OCH₃). ¹³C NMR (75 MHz, DMSO-*d*₆): δ 158.6 (C=O), 156.9 (N=C–N), 146.7 (C=N), 145.4 (C–NH), 136.1, 135.1 (2N=C=), 134.4, 133.2 (2CH Ar), 130.3, 127.4, 127.1, 127, 123.6, 121.6, 120.9, 119.8, 118.2, 116.2 (Ar), 114.9 (2CH Ar), 55.6 (OCH₃).

6-(*o*-Tolyl-hydrazono)-6H-indolo[2,1-*b*]quinazolin-12-one (3g)

Orange solid, M.p.: 230–232 °C, yield: 0.278 g (79%); IR (KBr) (ν_{\max} cm^{−1}): 3054 (NH), 2900 (=CH), 1687 (C=O), 1598, 1580 (C=C), 1545 (C–N), 1402 (C–NH), 1255, 1186 (C–N), 755 (Ar). ¹H NMR (300 MHz, DMSO-*d*₆): δ 13.82 (1H, s, NH), 8.54 (1H, d, 3J = 6.0 Hz, ArH), 8.42 (1H, d, 3J = 9.0 Hz, ArH), 7.85 (2H, t, 3J = 9.0 Hz, ArH), 7.76 (1H, d, 3J = 9.0 Hz, ArH), 7.69 (1H, d, 3J = 9.0 Hz, ArH), 7.59 (1H, t, 3J = 7.5 Hz, ArH), 7.43–7.33 (2H, m, ArH), 7.28 (1H, d, 3J = 9.0 Hz, ArH), 7.20 (1H, d, 3J = 6.0 Hz, ArH), 7.01 (1H, t, 3J = 3.0 Hz, ArH), 2.57 (3H, s, CH₃). ¹³C NMR (75 MHz, DMSO-*d*₆): δ 158.4 (C=O), 146.6 (N=C–N), 145.7 (C=N), 140.7 (C–NH), 136.8, 134.1 (2N=C=), 130.6, 128.1 (2CH Ar), 127.1, 127, 126.8, 126.7, 126.1, 124.3, 123, 121, 118.6, 116.7 (Ar), 112.8 (2CH Ar), 17.2 (CH₃). MS (EI): m/z (%) = 509 (0.2), 435 (1), 361 (4), 352 (M, 0.2), 326 (0.4), 281 (9), 253 (0.3), 234 (2), 207 (34), 187 (1), 162 (2), 133 (49), 96 (7), 64 (100), 44 (16).

8-Chloro-6-(*o*-tolyl-hydrazono)-6H-indolo[2,1-*b*]quinazolin-12-one (3h)

Orange solid, M.p.: 256–268 °C, yield: 0.348 g (90%); IR (KBr) (ν_{\max} cm^{−1}): 3019 (NH), 3000 (=CH), 1690 (C=O), 1599, 1555 (C=C), 1459 (C–N), 1263, 1191 (C–N), 750 (Ar), 677 (Cl–C). ¹H NMR (300 MHz, DMSO-*d*₆): δ 13.52 (1H, s, NH), 8.51 (1H, d, 3J = 9.0 Hz, ArH), 8.44 (1H, d, 3J = 9.0 Hz, ArH), 7.86 (2H, t, 3J = 9.0 Hz, ArH), 7.87–7.78 (4H, m, ArH), 7.55 (1H, t, 3J = 7.5 Hz, ArH), 7.40–7.21 (3H, m, ArH), 7.05 (1H, t, 3J = 6.0 Hz, ArH), 2.56 (3H, s, CH₃).

8-Bromo-6-(*o*-tolyl-hydrazono)-6H-indolo[2,1-*b*]quinazolin-12-one (3i)

Orange solid, M.p.: 274–276 °C, yield: 0.363 g (84%); IR (KBr) (ν_{\max} cm^{−1}): 3000 (NH), 2973 (=CH), 1685 (C=O), 1601, 1549 (C=C), 1463 (C–N), 1259, 1187 (C–N), 755 (Ar), 674 (Br–C). ¹H NMR (300 MHz, DMSO-*d*₆): δ 13.52 (1H, s, NH), 8.46 (1H, d, 3J = 3.0 Hz, ArH), 8.45 (1H, d, 3J = 3.0 Hz, ArH), 8.02 (1H, s, ArH), 7.88 (1H, d, 3J = 9.0 Hz, ArH), 7.80 (1H, d, 3J = 9.0 Hz, ArH), 7.75 (1H, d, 3J = 9.0 Hz, ArH), 7.55 (2H, d, 3J = 6.0 Hz, ArH), 7.32 (2H, d, 3J = 9.0 Hz, ArH), 7.06 (1H, s, ArH), 2.56 (3H, s, CH₃). MS (EI): m/z (%) = 509 (0.3), 430 (M, 82), 401 (14), 360 (3), 339 (9), 313 (76), 283 (9), 258 (9), 233 (17), 204 (60), 177 (40), 151 (11), 119 (63), 91 (100), 65 (6), 44 (24).

6-(*p*-Tolyl-hydrazono)-6H-indolo[2,1-*b*]quinazolin-12-one (3j)

Orange solid, M.p.: 286–288 °C, yield: 0.254 g (72%); IR (KBr) (ν_{\max} cm^{−1}): 3000 (NH), 2912 (=CH), 1683 (C=O), 1602, 1550 (C=C), 1492 (C–N), 1458 (C–NH), 1257, 1179 (C–N), 768 (Ar). ¹H NMR (300 MHz, DMSO-*d*₆): δ 13.49 (1H, s, NH), 8.59 (1H, d, 3J = 9.0 Hz, ArH), 8.46 (1H, d, 3J = 9.0 Hz, ArH), 7.88 (1H, d, 3J = 6.0 Hz, ArH), 7.81 (1H, d, 3J = 3.0 Hz, ArH), 7.57–7.51 (2H, m, ArH), 7.45 (1H, d, 3J = 9.0 Hz, ArH), 7.40–7.36 (4H, m, ArH), 7.22 (1H, d, 3J = 9.0 Hz, ArH), 2.37 (3H, s, CH₃). ¹³C NMR (75 MHz, DMSO-*d*₆): δ 158.7 (C=O), 146.9 (N=C–N), 145.9 (C=N), 140.3 (C–NH), 136.8, 134.2 (2N=C=), 133.3, 132.5 (2CH Ar), 130, 128, 127.3, 127, 126.2, 125.6, 124.6, 122.5, 121.2, 118.8, 116.8, (Ar), 114.5 (2CH Ar), 20.94 (CH₃).

8-Chloro-6-(*p*-tolyl-hydrazono)-6H-indolo[2,1-*b*]quinazolin-12-one (3k)

Orange solid, M.p.: 269–271 °C, yield: 0.306 g (79%); IR (KBr) (ν_{\max} cm^{−1}): 3000 (NH), 2913 (=CH), 1685 (C=O), 1604, 1549 (C=C), 1499 (C–N), 1310 (C–NH), 1258, 1182 (C–N), 770 (Ar). ¹H NMR (300 MHz, DMSO-*d*₆): δ 13.48 (1H, s, NH), 8.50 (1H, d, 3J = 9.0 Hz, ArH), 8.44 (1H, d, 3J = 9.0 Hz, ArH), 7.81 (3H, d, 3J = 6.0 Hz, ArH), 7.55 (1H, d, 3J = 6.0 Hz, ArH), 7.36 (3H, d, 3J = 9.0 Hz, ArH), 7.22 (1H, d, 3J = 6.0 Hz, ArH), 2.38 (3H, s, CH₃). ¹³C NMR (75 MHz, DMSO-*d*₆): δ 153.6 (C=O), 142 (N=C–N), 140.9 (C=N), 135.1 (C–NH), 130.1, 129.5 (2N=C=), 129, 127.2 (2CH Ar), 125.2, 122.8, 122.5, 122.3, 121.4, 119.5, 116.2, 114 (Ar), 113 (2CH Ar), 16.1 (CH₃).



8-Bromo-6-(*p*-tolyl-hydrazono)-6*H*-indolo[2,1-*b*]quinazolin-12-one (3l)

Orange solid, M.p.: 260–263 °C, yield: 0.319 g (74%); IR (KBr) (ν_{\max} cm⁻¹): 3100 (NH), 3018 (=CH), 1682 (C=O), 1602, 1550 (C=C), 1455 (C-N), 1312 (C-NH), 1259, 1182 (C-N), 769 (Ar). ¹H NMR (300 MHz, DMSO-*d*₆): δ 13.51 (1H, s, NH), 8.47 (1H, d, ³*J* = 3.0 Hz, ArH), 8.43 (1H, d, ³*J* = 3.0 Hz, ArH), 8.00 (2H, d, ³*J* = 3.0 Hz, ArH), 7.82 (1H, d, ³*J* = 3.0 Hz, ArH), 7.58–7.51 (2H, m, ArH), 7.39 (1H, d, ³*J* = 9.0 Hz, ArH), 7.23 (1H, d, ³*J* = 9.0 Hz, ArH), 2.38 (3H, s, CH₃). ¹³C NMR (75 MHz, DMSO-*d*₆): δ 158.5 (C=O), 146.8 (N=C-N), 145.6 (C=N), 139.9 (C-NH), 135.3, 134.3 (2N-C=), 133.8, 130.5 (2CH Ar), 130, 128.1, 127.2, 126.5, 124.2, 121.7, 120.9, 119.7, 118.2 (Ar), 114.6 (2CH Ar), 20.9 (CH₃).

Computational studies

DFT calculations: The DFT approach was used to compute the energies of FMOs and chemical reactivity descriptors based on FMOs for the synthesized quinazolin-12-one derivatives (3a–l). All DFT computations were performed using the B3LYP/6-31++G(d,p) level of theory and Gaussian 09W software; GaussView 6.0 was used to check files.³⁶

Molecular docking studies

The crystallographic structures of PDK1 (2R7B) were retrieved from the RCSB database. All protein docking preparations were conducted using the Protein Preparation Wizard,³⁷ where the protein was optimized, and missing residues were addressed. The synthesized derivatives were drawn using GaussView 6.0 and converted to pdb files for ligand preparation. The OPLS_2005 forcefield was applied to prepare the ligand at a pH of 7.0 ± 2.³⁸ Molecular docking simulations were performed using Schrödinger software,³⁹ specifically utilizing Glide with standard accuracy and flexible ligand sampling; 26 Å grid boxes were generated at each binding site and 10 poses were reported per ligand. The 2D and 3D interactions were visualized using BIOVIA Discovery Studio.⁴⁰

MD simulation

An MD simulation was performed utilizing Desmond software through the Schrödinger Maestro interface.⁴¹ The findings were consistent with those obtained from the earlier docking procedure involving the complex. The simulation cell was characterized as orthorhombic and was populated with water molecules according to the SPC model. Additionally, the system was supplemented with sufficient ions to neutralize the overall charge of the complex. The duration of the simulation was 100 ns, operating under the NPT ensemble framework. Throughout the simulation, the number of atoms remained constant, with the pressure maintained at 1.01325 bar and the temperature maintained at 300 K. The default thermostat employed was the Nose–Hoover chain method, with a 1.0 picosecond interval, whereas the Martyna–Tobias–Klein method served as the default barostat, set at a 2.0 picosecond interval. The MD simulation was evaluated using the Maestro simulation interaction diagram.

Evaluation of drug-likeness and *in silico* ADMET prediction

The approach utilized for assessing the drug-likeness and pharmacokinetic profiles of the synthesized quinazolin-12-one derivatives (3a–l) involved the SwissADME online platform.⁴² This methodology enabled the evaluation of several established drug-likeness criteria, including Lipinski's Ro5, Veber's Rule, Ghose's Rule, and Egan's Rule. These criteria were carefully applied to determine the drug-likeness profiles of the synthesized derivatives. Furthermore, *in silico* ADMET predictions were conducted using the ADMETlab 3.0 platform to analyze the absorption, distribution, metabolism, excretion, and toxicity of the compounds. This comprehensive strategy yielded valuable insights into the pharmacokinetic properties of the derivatives and their potential as promising drug candidates.

Data availability

All data generated or analyzed during this study are included in this published article and its ESI.†

Conflicts of interest

The authors declare that they have no known competing financial interests or personal relationships that could have appeared to influence the work reported in this paper.

References

- 1 H. Sung, J. Ferlay, R. L. Siegel, M. Laversanne, I. Soerjomataram, A. Jemal and F. Bray, Global cancer statistics 2020: GLOBOCAN estimates of incidence and mortality worldwide for 36 cancers in 185 countries, *Ca-Cancer J. Clin.*, 2021, **71**(3), 209–249.
- 2 X. Wu, Z. Yang, J. Zou, *et al.*, Protein kinases in neurodegenerative diseases: current understandings and implications for drug discovery, *Signal Transduct. Targeted Ther.*, 2025, **10**, 146.
- 3 A. Levina, K. D. Fleming, J. E. Burke and T. A. Leonard, Activation of the essential kinase PDK1 by phosphoinositide-driven trans-autophosphorylation, *Nat. Commun.*, 2022, **13**, 1874.
- 4 A. E. Leroux and R. M. Biondi, The choreography of protein kinase PDK1 and its diverse substrate dance partners, *Biochem. J.*, 2023, **480**(19), 1503–1532.
- 5 A. Glaviano, A. S. C. Foo, H. Y. Lam, *et al.*, PI3K/AKT/mTOR signaling transduction pathway and targeted therapies in cancer, *Mol. Cancer*, 2023, **22**, 138.
- 6 W.-H. Sun, Y.-H. Chen, H.-H. Lee, Y.-W. Tang and K.-H. Sun, PDK1- and PDK2-mediated metabolic reprogramming contributes to the TGFβ1-promoted stem-like properties in head and neck cancer, *Cancer Metab.*, 2022, **10**, 23.
- 7 J. Seo, J. Ha, E. Kang and S. Cho, The role of epithelial-mesenchymal transition-regulating transcription factors in anti-cancer drug resistance, *Arch. Pharm. Res.*, 2021, **44**(3), 281–292.



- 8 V. Serra, M. Scaltriti, L. Prudkin, *et al.*, PI3K inhibition results in enhanced HER signaling and acquired ERK dependency in HER2-overexpressing breast cancer, *Oncogene*, 2011, **30**(22), 2547–2557.
- 9 J.-J. Wang, M. K. Siu, Y.-X. Jiang, *et al.*, Aberrant upregulation of PDK1 in ovarian cancer cells impairs CD8⁺ T cell function and survival through elevation of PD-L1, *Oncoimmunology*, 2019, **8**(11), e1659092.
- 10 W.-H. Sun, Y.-H. Chen, H.-H. Lee, Y.-W. Tang and K.-H. Sun, PDK1- and PDK2-mediated metabolic reprogramming contributes to the TGFβ1-promoted stem-like properties in head and neck cancer, *Cancer Metabol.*, 2022, **10**, 23.
- 11 D. Arnaiz, J. Bryant, Y.-L. Chou, *et al.*, *US Pat.*, No. 07105563, Schering AG, 2006.
- 12 S. Faivre, G. Demetri, W. Sargent and E. Raymond, Molecular basis for sunitinib efficacy and future clinical development, *Nat. Rev. Drug Discov.*, 2007, **6**, 734–745.
- 13 I. Islam, J. Bryant, Y.-L. Chou, *et al.*, Indolinone based phosphoinositide-dependent kinase-1 (PDK1) inhibitors. Part 1: Design, synthesis and biological activity, *Bioorg. Med. Chem. Lett.*, 2007, **17**, 3814–3818.
- 14 I. Islam, G. Brown, J. Bryant, *et al.*, Indolinone based phosphoinositide-dependent kinase-1 (PDK1) inhibitors. Part 2: Optimization of BX-517, *Bioorg. Med. Chem. Lett.*, 2007, **17**, 3819–3825.
- 15 W. Zoubi and Y. Gun Ko, Schiff base complexes and their versatile applications as catalysts in the oxidation of organic compounds: Part I, *Appl. Organomet. Chem.*, 2017, **31**(3), e3574.
- 16 J. Mayans, D. Gómez, M. Font-Bardia and A. Escuer, Chiral oxazolidine complexes derived from phenolic Schiff bases, *Cryst. Growth Des.*, 2020, **20**(6), 4176–4184.
- 17 J. Ceramella, D. Iacopetta, A. Catalano, *et al.*, A review on the antimicrobial activity of Schiff bases: Data collection and recent studies, *Antibiotics*, 2022, **11**, 191.
- 18 S. Kaya, S. Erkan and D. Karakaş, Computational investigation of molecular structures, spectroscopic properties and antitumor-antibacterial activities of some Schiff bases, *Spectrochim. Acta, Part A*, 2021, **244**, 118829.
- 19 C. Verma and M. A. Quraishi, Recent progresses in Schiff bases as aqueous phase corrosion inhibitors: Design and applications, *Coord. Chem. Rev.*, 2021, **446**, 214105.
- 20 Y. B. Zambare, S. S. Chitlange and B. Bhole, Design and screening of PPAR-γ agonist based isatin derivatives and its remarkable activity as anti-cancer and anti-diabetic agents, *Res. J. Pharm. Technol.*, 2019, **4**, 2017–2026.
- 21 D. Iacopetta, R. Lappano, A. Mariconda, *et al.*, Newly synthesized imino-derivative analogues of resveratrol exert inhibitory effects in breast tumor cells, *Int. J. Mol. Sci.*, 2020, **20**, 7797.
- 22 Z. Q. Liao, C. Dong, K. E. Carlson, *et al.*, Triaryl-substituted Schiff bases are high-affinity subtype-selective ligands for the estrogen receptor, *J. Med. Chem.*, 2014, **57**(8), 3532–3545.
- 23 M. Chemchem, R. Menacer, N. Merabet, *et al.*, Green synthesis, antibacterial evaluation, and QSAR analysis of some isatin Schiff bases, *J. Mol. Struct.*, 2020, **1208**, 127853.
- 24 R. Purgatorio, N. Gambacorta, M. Catto, *et al.*, Pharmacophore modeling and 3D-QSAR study of indole and isatin derivatives as anti-amyloidogenic agents targeting Alzheimer's disease, *Molecules*, 2020, **25**, 5773.
- 25 R. Mishra, H. Chaurasia, V. Kumar, *et al.*, Molecular modeling, QSAR analysis, and antimicrobial properties of Schiff base derivatives of isatin, *J. Mol. Struct.*, 2021, **1243**, 130763.
- 26 Y. Belay, A. Muller, F. S. Mokoena, *et al.*, 1,2,3-Triazole and chiral Schiff base hybrids as potential anticancer agents: DFT, molecular docking and ADME studies, *Sci. Rep.*, 2024, **14**, 6951.
- 27 (a) D. Gheidari, M. Mehrdad and M. Bayat, Synthesis, molecular docking, molecular dynamics simulation, ADMET, drug-likeness, and DFT studies of novel Furo[2,3-b]indol-3a-ol as promising cyclin-dependent kinase 2 inhibitors, *Sci. Rep.*, 2024, **14**, 3084; (b) D. Gheidari, M. Mehrdad and M. Bayat, Novel indenopyrrol-4-one derivatives as potent BRDT inhibitors: Synthesis, molecular docking, drug-likeness, ADMET, and DFT studies, *J. Biomol. Struct. Dyn.*, 2024, 1–14; (c) D. Gheidari, M. Mehrdad and M. Bayat, Synthesis, molecular docking analysis, molecular dynamics simulation, ADMET, DFT, and drug-likeness studies: Novel Indeno[1,2-b]pyrrol-4(1H)-one as SARS-CoV-2 main protease inhibitors, *PLoS One*, 2024, **19**(3), e0299301; (d) N. Mahmoodi, M. Bayat, D. Gheidari and Z. Sadeghian, In silico evaluation of cis-dihydroxy-indeno[1,2-d]imidazolones as inhibitors of glycogen synthase kinase-3: Synthesis, molecular docking, physicochemical data, ADMET, MD simulation, and DFT calculations, *J. Saudi Chem. Soc.*, 2024, **28**(4), 101894; (e) F. Aghahosseinia, M. Bayat, Z. Sadeghiana, D. Gheidari and F. Safari, Synthesis, molecular docking study, MD simulation, ADMET, and drug-likeness of new thiazolo[3,2-a]pyridine-6,8-dicarbonitrile derivatives as potential anti-diabetic agents, *PLoS One*, 2024, **19**, e0299301.
- 28 M. A. E. El-Remaily, T. El-Dabea, R. M. El-Khatib, A. Abdou, M. A. El Hamd and A. M. Abu-Dief, Efficiency and development of guanidine chelate catalysts for rapid and green synthesis of 7-amino-4,5-dihydro-2-tetrazolo[1,5-a]pyrimidine-6-carbonitrile derivatives supported by density functional theory (DFT) studies, *Appl. Organomet. Chem.*, 2023, **37**(11), e7262.
- 29 Z. Sadeghian, M. Bayat and F. Safari, Synthesis and *in vitro* anticancer activity evaluation of spiro[indolo[2,1-b]quinazoline-pyrano[2,3-c]pyrazole] via sequential four-component reaction, *J. Mol. Struct.*, 2022, **1250**, 131759.
- 30 D. Gheidari, M. Mehrdad and F. Hosseini, Virtual screening, molecular docking, MD simulation studies, DFT calculations, ADMET, and drug likeness of diaza-adamantane as potential MAPK/ERK inhibitors, *Front. Pharmacol.*, 2024, **15**, 1360226.
- 31 H. M. Abd El-Lateef, M. M. Khalaf, F. El-Taib Heakal and A. Abdou, Fe(III), Ni(II), and Cu(II)-moxifloxacin-tri-substituted imidazole mixed ligand complexes: Synthesis, structural, DFT, biological, and protein-binding analysis, *Inorg. Chem. Commun.*, 2023, **158**(1), 111486.



- 32 A. M. El-Saghier, S. S. Enaili, A. M. Kadry, *et al.*, Green synthesis, biological and molecular docking of some novel sulfonamide thiadiazole derivatives as potential insecticidal agents against *Spodoptera littoralis*, *Sci. Rep.*, 2023, **13**, 19142.
- 33 RCSB Protein Data Bank. <https://www.rcsb.org>.
- 34 D. Gheidari, M. Mehrdad and Z. Karimelahi, Virtual screening, ADMET prediction, molecular docking, and dynamic simulation studies of natural products as BACE1 inhibitors for the management of Alzheimer's disease, *Sci. Rep.*, 2024, **14**, 26431.
- 35 L. Fu, S. Shi, J. Yi, *et al.*, ADMETlab 3.0: An updated comprehensive online ADMET prediction platform enhanced with broader coverage, improved performance, API functionality, and decision support, *Nucleic Acids Res.*, 2024, **52**(W1), W422–W431.
- 36 M. J. Frisch, G. W. Trucks, H. B. Schlegel, *et al.*, *Gaussian 09, Revision A.02*, Gaussian, Inc., Wallingford, CT, 2009.
- 37 Schrödinger. Protein Preparation Wizard, *Schrödinger Suite 2017-1*, New York, Schrödinger, LLC, 2017.
- 38 Schrödinger. LigPrep, *Schrödinger Release 2017-1*. New York, Schrödinger, LLC, 2017.
- 39 Schrödinger, *The Schrödinger Suite 2017-1*, New York, NY, 2017.
- 40 Dassault Systèmes, *BIOVIA Discovery Studio Visualizer*, San Diego, 2020.
- 41 S. Desmond. *Schrödinger Release 2017-1*, Schrödinger, LLC, New York, 2017.
- 42 A. Daina, O. Michielin and V. Zoete, SwissADME: A free web tool to evaluate pharmacokinetics, drug-likeness, and medicinal chemistry friendliness of small molecules, *Sci. Rep.*, 2017, **7**, 42717.

